

Journal of Fluid Mechanics

<http://journals.cambridge.org/FLM>

Additional services for *Journal of Fluid Mechanics*:

Email alerts: [Click here](#)

Subscriptions: [Click here](#)

Commercial reprints: [Click here](#)

Terms of use : [Click here](#)



Three-dimensional conditional structure of a high-Reynolds-number turbulent boundary layer

N. HUTCHINS, J. P. MONTY, B. GANAPATHISUBRAMANI, H. C. H. NG and I. MARUSIC

Journal of Fluid Mechanics / Volume 673 / April 2011, pp 255 - 285

DOI: 10.1017/S0022112010006245, Published online: 22 February 2011

Link to this article: http://journals.cambridge.org/abstract_S0022112010006245

How to cite this article:

N. HUTCHINS, J. P. MONTY, B. GANAPATHISUBRAMANI, H. C. H. NG and I. MARUSIC (2011). Three-dimensional conditional structure of a high-Reynolds-number turbulent boundary layer. Journal of Fluid Mechanics, 673, pp 255-285 doi:10.1017/S0022112010006245

Request Permissions : [Click here](#)

Three-dimensional conditional structure of a high-Reynolds-number turbulent boundary layer

N. HUTCHINS¹†, J. P. MONTY¹,
B. GANAPATHISUBRAMANI², H. C. H. NG¹
AND I. MARUSIC¹

¹Walter Bassett Aerodynamics Laboratory, Department of Mechanical Engineering,
University of Melbourne, Victoria 3010, Australia

²School of Engineering Sciences, University of Southampton,
Southampton SO17 1BJ, UK

(Received 17 February 2010; revised 9 November 2010; accepted 30 November 2010;
first published online 22 February 2011)

An array of surface hot-film shear-stress sensors together with a traversing hot-wire probe is used to identify the conditional structure associated with a large-scale skin-friction event in a high-Reynolds-number turbulent boundary layer. It is found that the large-scale skin-friction events convect at a velocity that is much faster than the local mean in the near-wall region (the convection velocity for large-scale skin-friction fluctuations is found to be close to the local mean at the midpoint of the logarithmic region). Instantaneous shear-stress data indicate the presence of large-scale structures at the wall that are comparable in scale and arrangement to the superstructure events that have been previously observed to populate the logarithmic regions of turbulent boundary layers. Conditional averages of streamwise velocity computed based on a low skin-friction footprint at the wall offer a wider three-dimensional view of the average superstructure event. These events consist of highly elongated forward-leaning low-speed structures, flanked on either side by high-speed events of similar general form. An analysis of small-scale energy associated with these large-scale events reveals that the small-scale velocity fluctuations are attenuated near the wall and upstream of a low skin-friction event, while downstream and above the low skin-friction event, the fluctuations are significantly amplified. In general, it is observed that the attenuation and amplification of the small-scale energy seems to approximately align with large-scale regions of streamwise acceleration and deceleration, respectively. Further conditional averaging based on streamwise skin-friction gradients confirms this observation. A conditioning scheme to detect the presence of meandering large-scale structures is also proposed. The large-scale meandering events are shown to be a possible source of the strong streamwise velocity gradients, and as such play a significant role in modulating the small-scale motions.

Key words: turbulent boundary layers

1. Introduction

The outer-layer structure of turbulent boundary layers has been explored by a variety of researchers. Initial insights were based upon spatio-temporal two-point

† Email address for correspondence: nhu@unimelb.edu.au

correlations. Statistics based on fluctuating streamwise velocity signals revealed the presence of large-scale low-frequency content in the log region (Kovaszny, Kibens & Blackwelder 1970; Blackwelder & Kovaszny 1972; Brown & Thomas 1977; Wark & Nagib 1991). The advent of laser diagnostics and numerical simulations has paved the way for the exploration of the spatial structure of wall-bounded turbulence. Particle image velocimetry (PIV) studies have revealed the presence of elongated low- and high-speed regions in instantaneous fields of streamwise velocity (Ganapathisubramani, Longmire & Marusic 2003; Tomkins & Adrian 2003). Hutchins & Marusic (2007a) used a spanwise rake of hot-wire probes and found that these elongated uniform momentum regions extend to large streamwise lengths and meander in the spanwise direction substantially. They used the collective term ‘superstructures’ to describe these events. Ganapathisubramani, Clemens & Dolling (2006, 2007, 2009) performed a variety of wide-field PIV and laser scattering measurements in streamwise/spanwise planes of a supersonic turbulent boundary layer and found similar elongated meandering features. These results are consistent with recent direct numerical simulation (DNS) studies performed by Ringuette, Wu & Martin (2008) in a Mach 3 supersonic boundary layer.

Very-large-scale structures have also been found in wall-bounded flows in internal geometries. In turbulent pipe flow, Kim & Adrian (1999) found peaks at long wavelengths in the pre-multiplied energy spectra of streamwise velocity fluctuations and termed these structures as ‘very-large-scale motions’ (VLSMs). Similar observations were also made in DNS of channel flow (del Álamo & Jiménez 2003; del Álamo *et al.* 2004). Subsequent studies in pipe and channel flows (Abe, Kawamura & Choi 2004; Guala, Hommema & Adrian 2006; Balakumar & Adrian 2007; Monty *et al.* 2007; Bailey *et al.* 2008) have confirmed the presence of these large-scale structures. Measurements within the atmospheric surface layer have also revealed the presence of surprisingly large elongated features (Young *et al.* 2002; Drobinski *et al.* 2004). In a scaled-up set of rake measurements in the near-neutral atmospheric surface layer, Hutchins & Marusic (2007a) and Marusic & Hutchins (2008) noted large-scale fluctuations that were quantitatively very similar to laboratory observed superstructure events.

Thus far, the view of these superstructure (or VLSM-) type motions has been distinctly two-dimensional in nature, formed exclusively from streamwise–spanwise data (notwithstanding the conditional averages of ‘passive wakes’ presented for channel flow DNS at $Re_\tau = 934$ in del Álamo *et al.* 2006). We here seek to extend the understanding of these events by measuring the three-dimensional structure associated with the largest scale events in turbulent boundary layers. Abe *et al.* (2004), Tsubokura (2005), Hutchins & Marusic (2007a) and Schlatter *et al.* (2009) have all noted that the large-scale events maintain a ‘footprint’ in the near-wall region. For this study, we intend to make use of this footprint in the fluctuating wall shear stress to detect the passage of superstructure events and enable the construction of a conditionally averaged view of these features.

Given the universal presence of these large-scale events, it is natural to consider their effect on other aspects of wall-bounded shear flows. In particular, the impact of large-scale structure on the near-wall signature must be explored. Previous studies have indeed examined this aspect. Rao, Narasimha & Narayanan (1971) examined the ‘bursting’ process and found that bursting might be a large-scale phenomenon in which the large outer-scaled structures interact with the near-wall structure. Bandyopadhyay & Hussain (1984) examined the relationship between large and small scales in numerous shear flows, including boundary layers, mixing layers,

wakes and jets. By studying short-time correlation measurements (from hot-wire time-series data) between the low-frequency component and a signal similar to the envelope of the high-frequency component, they found significant coupling between scales in all flows. Hunt & Morrison (2000) suggested that when the Reynolds number becomes sufficiently high, the large-scale features in the log layer become dominant and influence the near-wall region. They categorized this as a ‘top-down’ influence as opposed to the ‘bottom-up’ mechanism that is more commonly proposed from lower-Reynolds-number studies. More recently, Hutchins & Marusic (2007*b*) and Mathis, Hutchins & Marusic (2009) have suggested that the large-scale events modulate (or amplitude modulate) the small-scale fluctuations (such observations are in close agreement with earlier studies by Bandyopadhyay & Hussain 1984). Close to the wall, they noted that small-scale fluctuations were reduced within large-scale negative fluctuations. Further from the wall, this behaviour reversed, and small-scale fluctuations were found to be more energetic within large-scale negative fluctuations (this type of increased small-scale activity away from the wall within large-scale low-speed regions was also noted by Tanahashi *et al.* 2004 and del Álamo *et al.* 2006). We will here extend this work by monitoring the variation of the small-scale energy that is associated with the passage of large-scale skin-friction events.

2. Experiments

2.1. Facility

Experiments are performed in the high-Reynolds-number boundary layer wind tunnel at the University of Melbourne. This open-return blower wind tunnel has a 27 m long working section, with 2×1 m cross-sectional area. The pressure gradient is nominally zero, with pressure coefficient (C_p) variation along the entire 27 m length set to within ± 0.007 at a free-stream velocity, $U_\infty = 20 \text{ m s}^{-1}$. Further details of the facility are available in Nickels *et al.* (2005, 2007). During the current investigation, measurements were performed in the turbulent boundary layer developing over the tunnel floor at approximately 21 m downstream of the tripped inlet to the working section. The boundary-layer thickness (δ) at the measurement location was 0.326 m, as determined by fitting the mean velocity profile to a modified Coles law of the wall/wake formulation (see Perry, Marusic & Jones 2002). On average, this returns a boundary-layer thickness that is approximately 20 % greater than that determined using the δ_{99} criterion at this Reynolds number. The friction velocity, $U_\tau = 0.665 \text{ m s}^{-1}$, was calculated from a Clauser fit (Clauser 1956) to mean velocity data using log law constants $\kappa = 0.41$ and $A = 5.0$. On the basis of these values, the Kármán number, $Re_\tau = \delta U_\tau / \nu = 14\,200$ (where ν is the kinematic viscosity), while the Reynolds number based on momentum thickness, $Re_\theta = U_\infty \theta / \nu = 36\,980$. See table 1 for further details of the important boundary-layer parameters.

Throughout this paper, x , y and z will be used to denote the streamwise, spanwise and wall-normal axes, with u , v and w denoting the respective fluctuating velocity components. Capitalised velocities (e.g. U) or overbars (e.g. $\bar{u} = 0$) indicate time-averaged values. Tildes (e.g. \tilde{u}) denote conditionally averaged quantities. Time is denoted by t and the sample interval by Δt . The superscript ‘+’ is used to denote viscous scaling of length (e.g. $z^+ = z U_\tau / \nu$), velocity ($U^+ = U / U_\tau$) and time ($t^+ = t U_\tau^2 / \nu$). The shorthand $\partial_x A$ refers to the gradient of the quantity A in x (i.e. $\partial_x A = \partial A / \partial x$).

Re_τ	Re_θ	U_∞ (m s^{-1})	U_τ/ν (μm)	δ (m)	θ (m)	$1/\Delta t$ (Hz)	Δt^+	T (s)	TU_∞/δ
14 150	36 980	20.33	23	0.326	0.028	60 000	0.47	300	18 950

TABLE 1. Experimental conditions.

2.2. Measurement array

Two hot-wire probes, traversable in the wall-normal direction, are mounted above a spanwise array of 10 flush-mounted hot-film sensors affixed to the tunnel wall. The measurement array is shown in figure 1. The suffixes ‘hf’ and ‘hw’ will be used to denote the hot-film and hot-wire sensors, respectively. Table 2 details the important parameters of the measurement array.

2.2.1. Spanwise array

The spanwise array of hot-film sensors is located 21 m downstream of the inlet to the working section. The array covers a spanwise domain of $\sim 0.7\delta$, with a spanwise resolution $\Delta z_{hf} = 0.026 \text{ m}$ or 0.08δ . These sensors are Dantec 55R47 glue-on type and are operated in constant temperature mode using AA labs AN1003 anemometers with overheat ratio (OHR) set to approximately 1.05. The sensors are numbered sequentially from 1 to 10 as indicated in figure 1. The sensing element is a $0.1 \times 0.9 \text{ mm}$ (in x and y respectively) nickel film deposited onto a 0.05 mm thick insulating polyamide foil. The active spanwise length of the sensor l_{hf} (0.9 mm) equates to a viscous-scaled length $l_{hf}^+ = 39$ for this experiment. Though these sensor types are nominally referred to as ‘flush-mounted’, their attachment to the tunnel wall results in a small wall-normal step (due to the thickness of the polyamide foil and affixing tapes and glue). This step height has been measured with a wall-normal traversing microscope to be less than 0.075 mm. At $U_\infty = 20.33 \text{ m s}^{-1}$, this amounts to a viscous-scaled step height of approximately 3.35 wall units, which is very close to hydrodynamic smoothness (see, for example, Shockling, Allen & SMITS 2006, who showed no roughness effect for roughness heights less than ~ 3.5 wall units).

2.2.2. Traversing hot-wire probes

Two hot-wire probes are mounted with their sensing elements 220 mm upstream of the leading edge of a traversable sting. To minimise flow disturbance, the sting has an aerofoil profile (NACA0012) with chord length of 69.3 mm. The sting is mounted to a linear rail actuated by a ball screw and stepper motor arrangement. On the basis of the steps-per-revolution of the motor and the pitch of the ball screw, this computer-controlled sting could be traversed vertically with a minimum step size of $8 \mu\text{m}$. A Renishaw RG58C linear encoder provides a measurement of all incremental traverse movements with a resolution of $0.1 \mu\text{m}$. The boundary-layer traverse consists of 40 logarithmically spaced measurement stations within the range $0.2 < z < 450 \text{ mm}$.

The two hot-wire probes have prong spacing of 1 and 3 mm, with Wollaston wire soldered between the prongs. The etched sensor length for the two wires is 0.5 mm (wire diameter, $d = 2.5 \mu\text{m}$) and 1 mm ($d = 5 \mu\text{m}$), respectively. Both probes have a length to diameter ratio of 200, in keeping with recommendations from Ligrani & Bradshaw (1987) and Hutchins *et al.* (2009). Hot-wire sensors 1 and 2 are nominally mounted above hot-film sensors 5 and 6, respectively (see table 2 for precise locations). The hot wires are operated in constant temperature mode using AA labs AN1003 anemometers with an overheat ratio of 1.8.

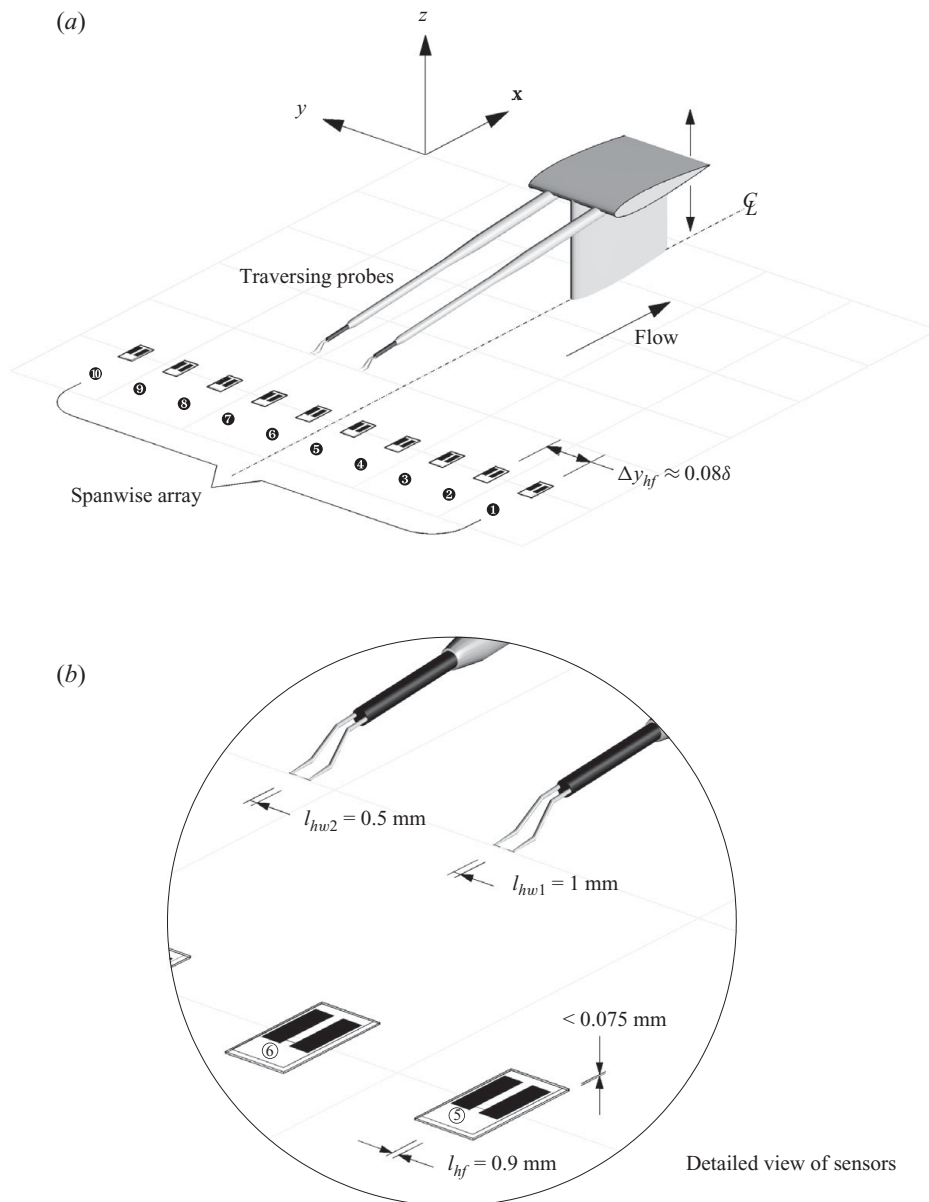


FIGURE 1. (a, b) Diagram detailing the measurement array.

The rationale for using two hot wires side-by-side is to obtain sufficient spatial resolution from the hot-wire measurements, whilst minimising errors due to drift. The authors have previously experimented with smaller wires and found them to often suffer from drift beyond the expected temperature drift (especially for long-duration experiments such as those attempted here). The longer $5 \mu\text{m}$ wire, however, has been found to drift only with ambient temperature variation, as it should. Therefore, the larger wire (hw1) is used to provide a reference mean velocity profile, to which the mean velocity of the calibrated smaller wire (hw2) may be forced, in order to

Array	Sensor		Location			Properties				
			x (m)	y (m)	z (mm)	l (mm)	l^+	d (μm)	l/d	OHR
Spanwise array	hf1	55R47	21	-0.117	0†	0.9	39	-	-	1.05
	hf2	55R47	21	-0.091	0	0.9	39	-	-	1.05
	hf3	55R47	21	-0.065	0	0.9	39	-	-	1.05
	hf4	55R47	21	-0.039	0	0.9	39	-	-	1.05
	hf5	55R47	21	-0.013	0	0.9	39	-	-	1.05
	hf6	55R47	21	0.013	0	0.9	39	-	-	1.05
	hf7	55R47	21	0.039	0	0.9	39	-	-	1.05
	hf8	55R47	21	0.065	0	0.9	39	-	-	1.05
	hf9	55R47	21	0.091	0	0.9	39	-	-	1.05
	hf10	55R47	21	0.117	0	0.9	39	-	-	1.05
Traversing probes	hw1	55P05	21	-0.015	z_1	1.0	44	5.0	200	1.8
	hw2	55P15	21	0.015	z_2	0.5	22	2.5	200	1.8

TABLE 2. Positions and dimensions of the sensors. †Nominally zero, the actual wall-normal location of the hot-film sensors is approximately 0.075 mm ($\approx 3\nu/U_\tau$) based on the worse-case measured thickness of the polyamide foil and fixing glue.

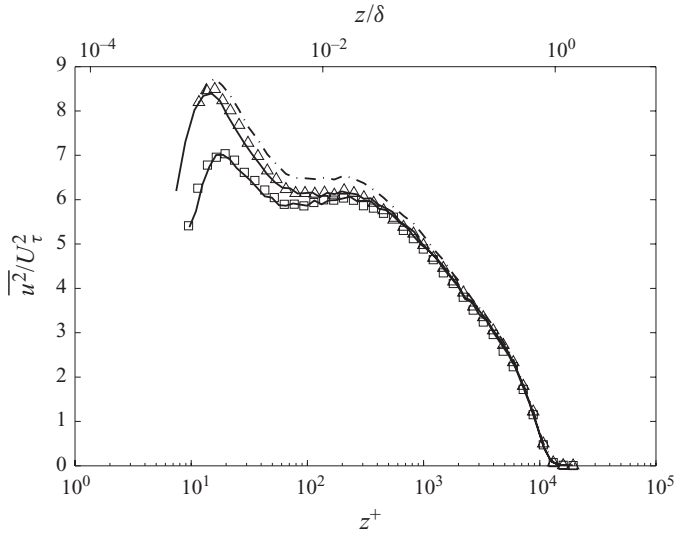


FIGURE 2. Broadband intensity profiles at $Re_\tau \approx 14150$ showing the effect of calibration correction on hw2. Symbols: \square , hw1 ($l^+ \approx 44$); \triangle , mean flow corrected hw2 ($l^+ \approx 22$). Dot-dashed line shows hw2 without mean flow correction. Solid lines show previous data from Hutchins *et al.* (2009) at comparable Reynolds number and l^+ ($Re_\tau = 13\,620$ and $13\,530$ and $l^+ = 22$ and 43).

determine a corrected calibration curve, and fluctuating statistics at each wall-normal location (see §2.3 for details of the initial hot-wire calibration). Figure 2 shows the result of this calibration correction for the smallest wire, showing that this technique is effective in accounting for unexpected drift in hw2. Unless otherwise stated, results presented in this paper are obtained from velocity data acquired from the 2.5 μm hot wire (hw2), nominally located over hot film 6. This wire is chosen since the larger wire suffers more severely from spatial resolution effects (see Hutchins *et al.* 2009),

although it is noted that data analysed from either wire would ultimately lead to the same conclusions.

2.3. Calibration

For calibration, the traversing hot-wire probe is positioned in the free stream and statically calibrated *in situ* against a Pitot-static tube pair before and after each boundary-layer traverse. Third-order polynomial curves are fitted to the calibration data. Atmospheric conditions are monitored continuously throughout the experiments using a calibrated thermocouple and an electronic barometer. Linear interpolation between the pre- and post-calibration curves is used to correct for temperature change during the course of the experiment.

During the hot-wire anemometer calibration process, the 10 wall-mounted glue-on sensors are also simultaneously sampled, such that mean voltages are obtained from each hot-film sensor as a function of U_∞ . Using existing data obtained in the same facility (Mathis *et al.* 2009), it is possible to obtain an approximate expression for friction velocity U_τ as a function of Re_x ($U_\infty x/\nu$). This empirical expression has the approximate form

$$U_\tau = U_\infty / (C_1 + C_2 \log Re_x), \quad (2.1)$$

which assumes that U_∞/U_τ varies logarithmically with Reynolds number (a best fit to this formula suggests $C_1 \approx -1.23$ and $C_2 \approx 1.86$). It is noted that there is considerable uncertainty in this approximation: for the experimental data used in formulating (2.1), U_τ is obtained using the Clauser technique (based on the constants $\kappa = 0.41$ and $A = 5.0$). However, any such errors in this calibration technique will have minimal effect on the analysis to follow, for which the spanwise array is used *only* to detect the occurrence of large-scale positive or negative streamwise velocity events. In the same manner as for the hot-wire calibration, a linear interpolation between the hot film pre- and the post- calibration is used to correct for temperature change during the experiment.

A test for possible interference between the hot wires and the hot films has also been conducted. The hot films are operated at very low OHRs, and as such are not observed to interfere with the operation of the hot-wire sensors (even when the hot wires are very close to the wall). The measured hot-wire statistics match those previously taken in this same facility in the absence of the spanwise array of hot-film sensors (see Hutchins *et al.* 2009). Potentially of more concern here is that the hot-wire sensors (which are operating at quite high temperatures, with an OHR of 1.8) could interfere with the immediately adjacent hot-film sensors when in wall proximity. There is a 2.5% change in the mean skin friction recorded by hf6 in proximity to hw2 (this effect abates completely once the hot wire is more than 10 mm from the surface). This is effectively just a mean shift which is subtracted for all subsequent analyses (where only the fluctuating part of the hot-film signal is used) and hence does not influence results. There is no similar trend discernible in the turbulence intensity. A study of the energy spectra from the hot film for various hot-wire locations reveals no overall change in hot-film statistics as a function of proximity and therefore it is concluded that, for the purposes of this study, there is no discernible interference between the hot wire and hot film.

3. Frequency response of skin-friction sensors

Figure 3(a) shows a short example signal from the hot-wire sensor hw2 at $z_2^+ = 11$ (the closest position to the wall) and from hf6, the hot-film sensor almost directly

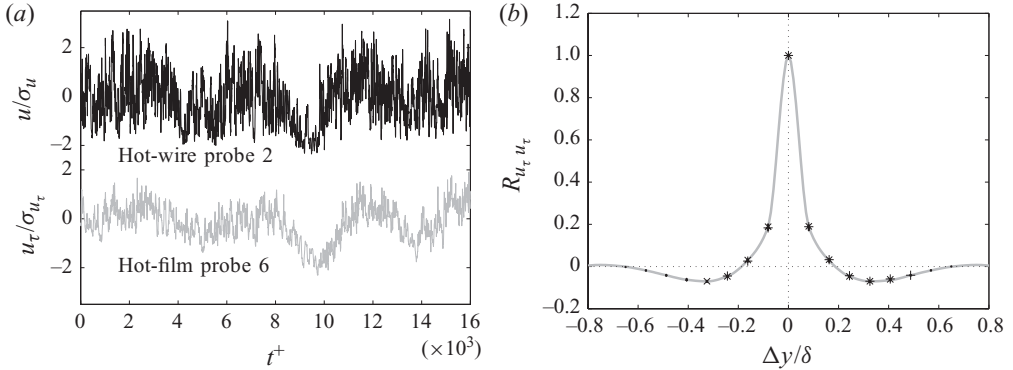


FIGURE 3. (a) Time series of skin-friction fluctuations from hf6 (grey) and velocity fluctuations from hw2 at $z^+ = 11$. The data were obtained simultaneously at the same acquisition rate with the hot-wire located directly above the glue-on probe. (b) Two-point correlation of measured skin-friction fluctuations between: (+) hf4 and all other sensors, (\times) between hf5 and all other sensors, and (\bullet) all sensors in the spanwise array.

beneath hw2 (see table 2 for exact probe locations). It is observed that the large-scale components of these two signals appear well correlated. The overall correlation with zero time-shift between the two signals shown is 0.3, and over 93 % of this correlation occurs in the frequency range $f < 80$ Hz (this corresponds to streamwise wavelengths of $\lambda_x > 0.5\delta$). However, it is noted that there is a large discrepancy between the magnitude of the small-scale fluctuations. The hot wire clearly captures more small-scale information than the hot film. Bruun (1995) gave a good introduction to the problems associated with these type of hot-film sensors. In general, for wall-mounted sensors, in addition to heat lost from the sensor element to the airflow (which is used to infer skin friction), there is also substantial heat loss to the substrate (the tunnel wall). This heat conducted into the substrate is significantly greater than that lost to the flow by forced convection, and thus only a small proportion of the fluctuating signal is flow-dependent. Additionally, the overall frequency response of the system (and hence the ability of the hot films to capture small-scale fluctuations) is also considerably reduced due to the large thermal inertia of the substrate. The end result is a reduced measured magnitude of skin-friction fluctuations, as clearly shown by comparison with previous investigations: the hot-film sensors indicate a standard deviation of just 7 %, while DNS data at $Re_\tau \approx 934$ indicate a value of approximately 20 % (del Álamo *et al.* 2004). A similar value for root-mean-squared deviations of U_τ fluctuations was also suggested by Alfredsson *et al.* (1988) and Kunkel & Marusic (2003).

Since the hot films are only used as a ‘detector’ probe for the large-scale events, the precise value of the standard deviation and any attenuation of small scales will be of little impact to the proceeding analysis. It is only the shape and size of the correlated large-scale events across the array that are of interest, and these are noted to be consistently well captured by the array. Figure 3(b) shows the cross-correlation of the skin-friction fluctuations across the spanwise array,

$$R_{u_\tau u_\tau}(i, j) = \frac{\overline{(u_{\tau_{hf_i}} u_{\tau_{hf_j}})}}{\sigma(u_{\tau_{hf_i}})\sigma(u_{\tau_{hf_j}})}, \quad (3.1)$$

where i and j are sensor numbers 1–10, $u_{\tau_{hf_i}}$ is the fluctuating friction velocity time-signal as measured by sensor i , and σ is the standard deviation of this time signal.

The plus symbols show hf4 correlated with all other sensors ($i = 4, j = 1, 2, 3, \dots, 10$), the cross symbols show hf5 correlated with all other sensors ($i = 5, j = 1, 2, 3, \dots, 10$). The solid dot symbols show all other combinations. It can be seen that the cross-correlation profiles agree well for all values of i , indicating that, in spite of obvious attenuation and conduction to the substrate, all 10 sensors are behaving in a consistent manner. The shape of the correlation curves in figure 3(b) is also entirely consistent with previous literature. The observed positive peak and negative troughs separated by $O(\delta)$ are a well-known characteristic of larger-scale events further from the wall; very similar behaviour of the streamwise velocity fluctuations in the logarithmic region has been documented by Hutchins & Marusic (2007a) and Monty *et al.* (2007). More recently, Schlatter *et al.* (2009) have shown a similar pattern for the wall shear stress correlation. They observed $0.85\delta_{99}$ separating the negative troughs for $R_{\tau\tau}$ (where δ_{99} is the boundary-layer thickness based on 99 % of free-stream velocity). Allowing for the fact that δ_{99} is approximately 20 % less than that computed from the modified Coles fit used here (i.e. $\delta_{99} \approx 0.8\delta$), the separation between negative troughs in figure 3(b) is very close to this value.

The comparison of the spectral content between hf6 and hw2 in figure 3(a) clearly shows that the large-scale information from the skin-friction sensors is correct whilst the high-frequency energy content is clearly attenuated (and possibly spurious). In light of this, the friction velocity signals from the spanwise array are filtered using a two-dimensional Gaussian (with approximate length 0.5δ and spanwise width 0.16δ) to leave only the large-scale component of the signal (in terms of the time-series data this equates to filtering information from the skin-friction signals for which $f \gtrsim 80$ Hz). The overall zero time-shift correlation between the filtered hf6 and hw2 is increased to 0.35 as a result of the filtering process.

4. Convection velocity

To infer length-scale information from the time-series hot-film array data, it is necessary to assume a convection velocity U_c . It is common practice to use the local mean velocity U of the time-series data for this purpose. However, for the hot-film array, which is approximately flush-mounted, the local mean is diminishingly small. Close to the wall, one would expect the convection velocity to be much larger than the local mean (for example, see Kreplin & Eckelmann 1988). In addition, one would also expect this convection velocity to be scale dependant. Large-scale events (such as the highly elongated structure visible in figure 5) are the footprints of events that originate in the logarithmic region, and hence would be expected to convect with high U_c (close to the mean velocity in the log region). Smaller-scale structures, of the order of 1000 wall units in length, are due to the near-wall cycle which originates at $z^+ \approx 15$. Hence, these would be expected to advect with a slightly lower convection velocity, close to the mean at $z^+ = 15$ ($U_c^+ \approx 11$). Monty & Chong (2009) and del Álamo & Jiménez (2009) have recently presented evidence of such scale-dependent convection velocities in wall-bounded turbulence.

In the current study, since we are most interested in the large-scale motions (and indeed most of the small-scale information is not resolved or removed from the hot-film signals by the Gaussian filtering), the appropriate convection velocity to use is the speed with which the large-scale events (say, $\lambda_x \geq \delta$) advect. This convection velocity has been measured by rotating the spanwise array of hot films through 90° , such that it forms a streamwise array with hot-film probe 1 as the most upstream sensor (the hot-film array is actually mounted on a 350 mm diameter plug installed in the tunnel

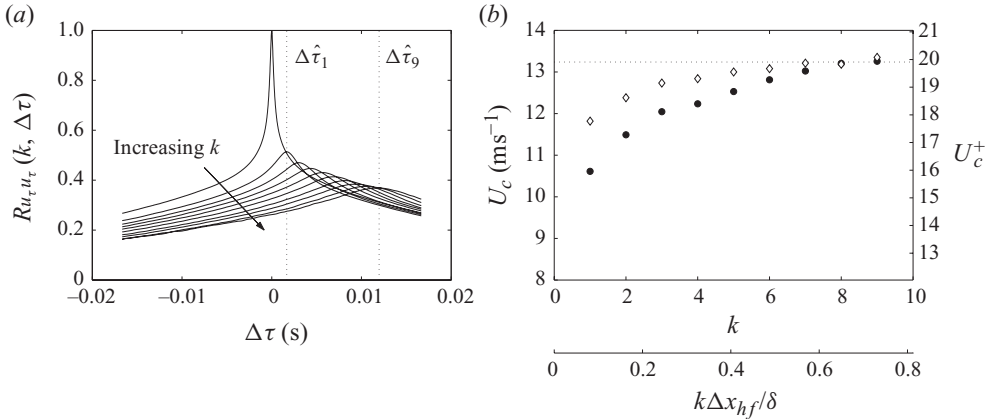


FIGURE 4. Determining the convection velocity U_c from the streamwise hot-film array: (a) cross-correlation $R_{u_\tau u_\tau}(k, \Delta\tau)$ as a function of the time shift $\Delta\tau$ for probe separation $k=0$ to 10, vertical dotted lines show time shift for maximum correlation ($\Delta\hat{\tau}_k$) for $k=1$ and $k=9$; (b) U_c as a function of probe separation for (solid symbols) unfiltered and (open symbols) Gaussian-filtered data. Horizontal dotted line shows (4.2) evaluated at the appropriate Kármán number.

wall, and thus this process is relatively simple). Figure 4(a) shows the cross-correlation between probe hf_i ($i=1, 2, 3, \dots, 10$) and probe hf_j ($j=i, i+1, i+2, \dots, 10$) as a function of time-shift $\Delta\tau$,

$$R_{u_\tau u_\tau}(k, \Delta\tau) = \frac{\overline{u_{\tau_{hf_i}}(t) u_{\tau_{hf_j}}(t + \Delta\tau)}}{\sigma(u_{\tau_{hf_i}}) \sigma(u_{\tau_{hf_j}})}, \quad (4.1)$$

where $k=j-i$ and denotes the number of probe spacings ($\Delta x_p = 26$ mm) separating the cross-correlated signals. The time shift at which the maximum correlation occurs is defined as $\Delta\hat{\tau}_k$. Example maximum time shifts for $k=1$ and $k=9$ are shown in figure 4(a) by the dotted lines. The convection velocity is defined as $U_c(k) = k\Delta x_p / \Delta\hat{\tau}_k$. The solid symbols in figure 4(b) show this convection velocity as a function of probe separation $k\Delta x_p$ for all nine probe spacings. It is noted that the convection velocity increases with increasing probe separation k , which is indicative of a scale-dependent U_c . For small probe separations, there will be correlated information between hf_i and hf_j over a broad range of scales, including small scales. This small-scale information will tend to move slower than the large-scale information as it is centred closer to the wall. Consequently, we expect lower values of U_c for smaller k .

Conversely, for larger k , it is predominantly the large-scale information that is correlated between hf_i and hf_j . Since the large-scale information at the wall is believed to be the footprint of log region structures, it is logical to expect these features to advect with a faster speed (equal to a local mean in the log region). As further proof that U_c is scale-dependent, the open symbols in figure 4(b) show the convection velocity as determined from the Gaussian-filtered hot-film signals. In this case, most of the small-scale information has been removed from the hot-film signals, and it is noted that for small probe separations, the convection velocities indicated by the filtered hot-film signals are faster. At the maximum probe separation ($k=9$, equating to a streamwise separation of $\approx 0.7\delta$), the measured U_c for both the filtered and unfiltered data appears to be converging to a common value.

Mathis *et al.* (2009) have observed that the wall-normal location for the outer peak in the energy spectra (due to the very-large-scale superstructure-type events) occurs at $z^+ \approx \sqrt{15Re_\tau}$ across a large range of Reynolds numbers ($4000 \lesssim Re_\tau \lesssim 19\,000$). This is the geometric midpoint of the log region (in log space) assuming the limits $100 < z^+ < 0.15\delta^+$. The mean velocity at this height (which one might suppose could indicate the convection velocity for these large-scale events) can be estimated based on the log law as

$$U_c^+ \equiv U^+ = \frac{1}{\kappa} \ln \sqrt{15Re_\tau} + A. \quad (4.2)$$

The dotted horizontal line in figure 4(b) shows (4.2) evaluated for $Re_\tau = 14\,150$ (the boundary layer examined in the present study). This value is very close to the measured U_c at the maximum probe separation. Therefore, this value of convection velocity is used to examine the large-scale features.

The results in figure 4 have implications for any attempt to present time-series data in spatial or wavenumber domain. Not only is the convection velocity scale-dependant, but also the spread of convection velocities in the near-wall region will increase with Reynolds number (as the scale separation increases). The near-wall scales would be assumed to convect at a fixed viscous-scaled velocity based, say, on the mean at $z^+ = 15$ ($U_c^+ \approx 11$). Equation (4.2) indicates that the convection velocity for the large-scales is Reynolds number dependent. This implies that the ratio of convective velocities between the superstructure and the near-wall cycle may approximately follow

$$\frac{1}{9} \log Re_\tau + \frac{3}{4}. \quad (4.3)$$

As an example, this ratio would be a factor of 1.5 at $Re_\tau \approx 1000$, increasing to 2 at $Re_\tau \approx 73\,000$, and for atmospheric type Reynolds numbers would attain a ratio of approximately 2.3. Using DNS data of turbulent channel flow, del Álamo & Jiménez (2009) calculated scale dependent convection velocities noting a very similar behaviour. They found a small-scale convection velocity that remains approximately fixed at $U_c^+ \approx 11$ and a large-scale convection velocity that is a fixed proportion of the bulk velocity (U_b) and would hence scale as $\sim \log Re_\tau$. This would imply a similar ratio between small- and large-scale convection velocity to that given in (4.3)

5. Large-scale skin-friction fluctuations

Having identified an approximate convection velocity for the large-scale structure, the skin-friction fluctuations from the spanwise array can be used together with Taylor's hypothesis to present a pseudo-spatial snapshot of the large-scale events at the wall. The advantage of projecting time-series data using Taylor's hypothesis is that we can discuss characteristic length scales (rather than time scales) in the flow which enables a more intuitive approach later in the text when we consider the modulating link between large- and small-scale events. In figure 5, a streamwise–spanwise plane is reconstructed using a convection velocity equal to $20U_\tau \approx 0.65U_\infty$ as determined from (4.2). The plot shows the presence of meandering elongated low and high shear-stress regions. Abe *et al.* (2004) found similar very-large-scale skin-friction fluctuations in DNS of turbulent channels (for $Re_\tau \leq 640$). Figure 5(a) shows the raw unfiltered data. In this plot, these elongated regions clearly have noisy smaller scale fluctuations within. These small scales are unreliable and can be removed using the Gaussian filter discussed in § 3. Figure 5(b) displays the filtered skin-friction fluctuations, more clearly revealing the elongated, large-scale, low skin-friction region (blue) located between high skin-friction regions (red). A number of previous studies have reported similar

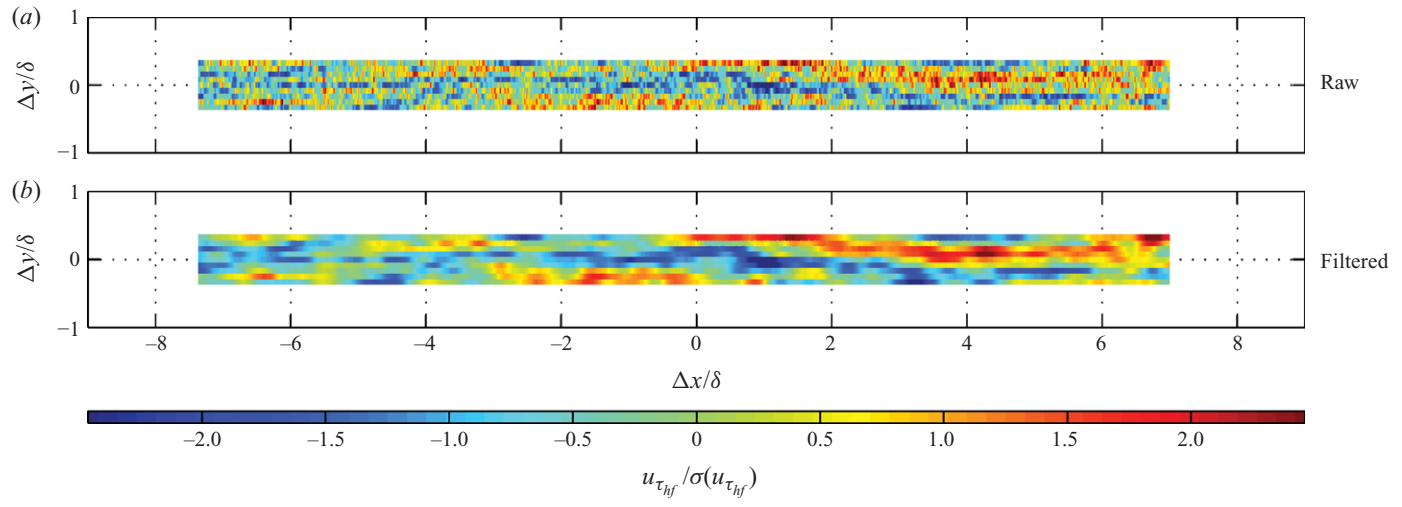


FIGURE 5. Example fluctuating friction velocity signals from the spanwise array: (a) unfiltered raw data; (b) 2D Gaussian filter of size $0.5\delta \times 0.16\delta$ (streamwise and spanwise) applied. Colour shows fluctuating skin-friction velocity normalised by the standard deviation. Signals are projected in x using Taylor's hypothesis and a convection velocity of $U_c^+ = 20$.

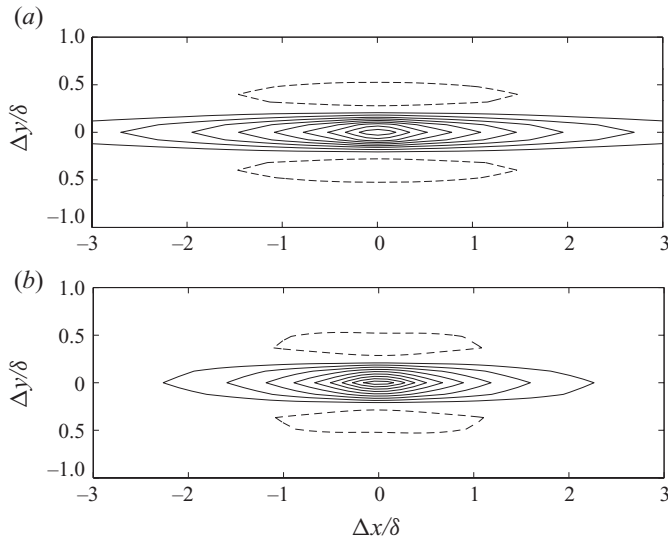


FIGURE 6. (a) Two-point correlation map from the skin-friction sensor array; (b) comparison two-point correlations from hot-wire rake data at $z/\delta = 0.05$ and $Re_\tau = 14\,380$ (Hutchins & Marusic 2007a). Both sets of data are filtered with the same Gaussian filter (with approximate length 0.5δ and spanwise width 0.16δ) as described in §3. Contours show R_{uu} from -0.2 to 1.0 with 0.1 increment. Solid contours show positive R_{uu} and dashed contours show negative. Zero contour is omitted.

patterns of relatively low- and high-speed velocity regions in the logarithmic region of wall-bounded turbulent flows over a wide range of Reynolds and Mach numbers (Ganapathisubramani *et al.* 2006; Monty *et al.* 2007; Hutchins & Marusic 2007a).

Figure 6(a) shows a two-dimensional representation of the two-point correlation for the Gaussian-filtered skin friction. For comparison, figure 6(b) shows comparable data from the hot-wire rake measurements of Hutchins & Marusic (2007a). These data are at comparable Reynolds number, and a similar Gaussian filter has been applied; however, the rake is located in the log region. Despite this, the two correlation maps are qualitatively strikingly similar. A region of elongated positive correlation is flanked on either side by anti-correlated behaviour with the spanwise width separating the anti-correlated lobes similar in both cases ($\approx 0.7\text{--}0.8\delta$). Quantitatively, the correlations are slightly longer for the skin friction than exhibited by the log-region velocity signals. This is to be expected, however, since the length of the large-scale structures seems in general to increase substantially as we approach the wall (see figures in §6.2).

In summary, elongated and meandering low and high skin-friction regions at the wall exist and share sufficient similarities such that they are almost certainly related to the large-scale superstructures in the logarithmic region. These results further confirm the findings of §3, namely the hot-film sensor array is deemed suitable for its intended purpose, which was simply to detect the passage of such large-scale fluctuations. In the following analyses, the detection of such large-scale events will provide a condition vector for conditional averaging of the more accurate hot-wire sensor.

6. Conditional events

The relationship between the skin-friction fluctuations and the velocity fluctuations can be examined by computing conditional quantities from the hot-wire probe

conditioned in the presence of a low/high skin-friction event. A low skin-friction event occurs when the instantaneous skin-friction fluctuation is less than zero and conversely a high skin-friction event occurs when the fluctuation is greater than zero. Note that no thresholds are used anywhere in this analysis; events are discriminated only on sign. Because the wall shear stress and streamwise velocity data are acquired simultaneously, the conditional average defined as

$$\tilde{u}|_l(\Delta t, \Delta y, z) = \langle u(t, y, z) \mid u_\tau(t - \Delta t, y - \Delta y) < 0 \rangle \quad (6.1)$$

is a function of the wall-normal, spanwise and temporal separation. Applying Taylor's hypothesis with $x = -U_c t$ converts the conditional average to a function of all three spatial coordinates:

$$\tilde{u}|_l(\Delta x, \Delta y, z) = \langle u(x, y, z) \mid u_\tau(x - \Delta x, y - \Delta y) < 0 \rangle \quad (6.2)$$

for the low shear-stress event and

$$\tilde{u}|_h(\Delta x, \Delta y, z) = \langle u(x, y, z) \mid u_\tau(x - \Delta x, y - \Delta y) \geq 0 \rangle \quad (6.3)$$

for the high shear-stress event. In these equations, u is the fluctuating streamwise velocity and u_τ is the friction velocity fluctuation about the unconditional mean friction velocity U_τ . Here, U_c is the convection velocity chosen to be $0.65U_\infty$ (13.2 m s^{-1}), as discussed in §4. Note that the Gaussian-filtered skin friction is used for conditioning rather than the unfiltered signal. Filtering is applied to avoid conditioning on small-scale skin-friction events, since it is the aim of this paper to examine the flow around large-scale low and high friction events.

6.1. *At the origin*

Figure 7(a) shows the conditional mean velocity profiles ($U + \tilde{u}$) computed using hot-film sensor 6 and the hot wire (hw2) that is located almost directly above it (i.e. $\Delta y \approx 0$). The unconditional mean velocity profile is plotted together with the conditional quantities for low and high skin-friction events. The velocity statistics are scaled with the unconditional mean friction velocity, U_τ ($= 0.665 \text{ m s}^{-1}$). It is immediately clear from figure 7(a) that a low skin-friction event is associated with a velocity profile that is consistently lower than the unconditional mean throughout the near-wall and logarithmic regions. Similarly, a high skin-friction event has a velocity profile that is consistently higher. The two conditional profiles collapse onto the unconditional profile beyond $y/\delta \approx 0.5$, suggesting large-scale events having a connection with (or footprint at) the wall are not statistically influenced by (and do not influence) the outer wake region of the boundary layer.

The conditional streamwise velocity fluctuation (based on a low skin-friction event) $\tilde{u}^+(0, 0, z)$ is displayed in figure 7(b). It is apparent that the greatest deviation from the unconditional mean does not occur nearest the wall, but at a location in the logarithmic region. The difference grows from the wall into the log region, where a plateau is reached before the conditional velocity approaches the unconditional mean as we move into the outer region. The plateau of maximum conditional mean deviation occurs between $z \approx 0.01 - 0.03\delta \approx 140 - 400\nu/U_\tau$, with an arguable peak at $z = 0.02\delta = 280\nu/U_\tau$. The fact that the deviation has a maximum magnitude away from the wall could indicate that the source of the large-scale low or high skin-friction event is in the logarithmic region. This result once again highlights the interaction or footprint of outer-scaled superstructures at the wall.

The aforementioned plateau in conditional–unconditional velocity difference implies that a logarithmic region of the conditional mean velocity profiles exists. This certainly

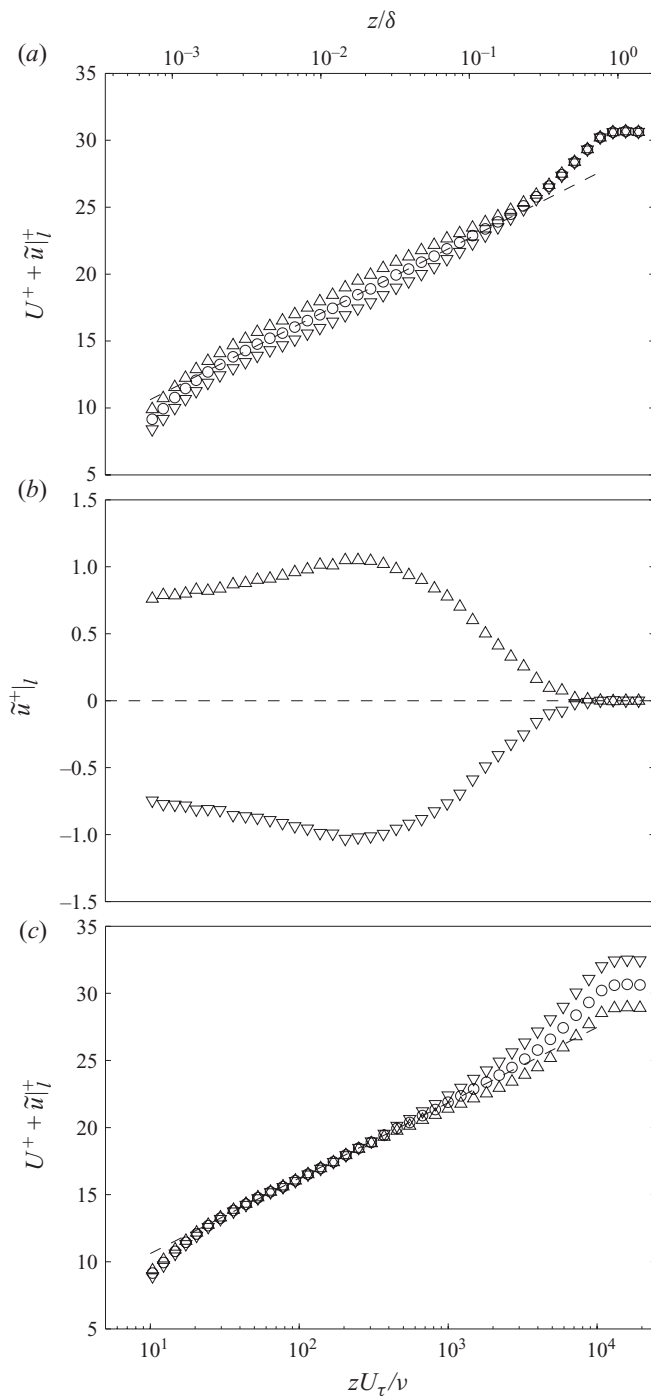


FIGURE 7. (a) Wall-normal velocity profiles at zero time shift: unconditional (\circ) and conditionally averaged on low (∇) and high shear-stress (\triangle) events. (b) Difference between conditional and unconditional velocity profiles, \tilde{u} . (c) Velocity profiles rescaled with conditional U_τ .

appears visually evident in figure 7(a). If this is really so, then a rescaling of the conditional velocity profiles could lead to collapse in the log region of the flow. The rescaling could be forced by assuming the same logarithmic law for conditional and unconditional profiles (and attempting a Clauser fit). However, this is unnecessary here since the acquired experimental data provides the fluctuating skin-friction directly. Therefore, it is possible to calculate the conditionally averaged friction velocities

$$\begin{aligned}\widetilde{U}_\tau|_l &= \langle u_\tau(0, t) + U_\tau \mid u_\tau(0, t) < 0 \rangle, \\ \widetilde{U}_\tau|_h &= \langle u_\tau(0, t) + U_\tau \mid u_\tau(0, t) \geq 0 \rangle,\end{aligned}\tag{6.4}$$

and these new velocity scales can be used to rescale the conditional velocity profiles. It was found that $\widetilde{U}_\tau|_l = 0.623$ and $\widetilde{U}_\tau|_h = 0.699$, meaning the local mean friction velocity is reduced by 5.7% during periods of low skin friction and increased by 5.9% when skin friction is relatively high. Figure 7(c) displays the result, showing excellent collapse of the conditional velocity profiles up to approximately $z = 0.03\delta$ ($z^+ \approx 400$).

The rescaled velocity profiles show trends normally associated with non-zero pressure-gradient boundary layers. That is, the velocity profile above low skin-friction regions resembles an adverse-pressure-gradient turbulent boundary layer, having a strong wake (high scaled mean velocity for $z/\delta \gtrsim 0.1$) and lower friction velocity; whereas the mean flow over a high wall shear-stress event resembles that of a favourable pressure gradient layer (and consistent with this observation, the weaker wake and extended logarithmic region for this high wall shear case also more closely resembles the velocity profile associated with internal geometries). Considering that it has been shown by Hutchins & Marusic (2007a) that large-scale, low-speed events are preceded and followed by large-scale high-speed events, it is conceivable that the flow inside the large-scale structure is experiencing a significant local pressure gradient. A further interpretation of figure 7(c) is that the flow near to the wall experiences local Reynolds number changes, varying by approximately $\pm 6\%$ due to the passage of large-scale events.

Regardless of the reasons for the noted behaviour, the conditional scaling of the near-wall flow may have implications for near-wall control strategies and near-wall turbulence models. If we subscribe to top-down-type structural models, these results would seem to reaffirm that the passage of very-large-scale logarithmic features can cause substantial large-scale modification to skin friction at the wall.

6.2. Three-dimensional view

In addition to the zero time-shift results shown above, the simultaneous acquisition of skin-friction and hot-wire time series allows us to compute conditionally averaged velocity profiles that occur before or after a low or high skin-friction event. Moreover, although the hot-wire probe is located above hot-film 6, hot-films 1–5 and 7–10, together with the hot-wire signal, can be used to determine the spanwise-wall-normal signature of the conditional structure (see (6.1)–(6.3)). Figure 7(b) and other three-dimensional data analyses (not shown here for brevity) clearly show that low-speed conditional averages are, for the purposes of this investigation, simply the negative of the high-speed conditional averages. This trend has been observed throughout our analysis of the large-scale conditional events. For this reason, and because superstructures were first identified by their low-momentum signature (Hutchins & Marusic 2007a), only three-dimensional representations of *low* skin-friction conditional averages are shown in this paper.

Figure 8 shows iso-contours of $\tilde{u}|_t^+$ in various x - y , y - z and x - z planes. The x - z plane is extracted along $\Delta y = 0$ and the x - y plane shown is located at $z/\delta = 7 \times 10^{-4}$ (the closest position to the wall from the hot-wire traverse). In figure 8(a), three y - z planes at $\Delta x/\delta = 0, 1, 2$ are also shown to give a three-dimensional view of a characteristic large-scale low-speed event. Note that two views are shown; one with linear scaling of the z -axis and the other with logarithmic scaling in an effort to highlight features of the structure both near the wall (log) and in the outer region (linear). The figures reveal an inclined, forward-leaning, low-speed structure extending beyond 3δ in the downstream direction and 2δ upstream. The features of this structure are generally consistent with various other studies in the literature (Kovaszny *et al.* 1970; Brown & Thomas 1977, among others). In the spanwise direction (y - z planes), there is a clear high–low–high conditional velocity behaviour, also documented previously through two-point correlations. This trend begins at the wall and extends well out into the outer region (recall that the skin-friction correlation in figure 6 also showed this trend). The width of the low-speed region appears to be approximately 0.5δ at $\Delta x = 0$. This width and the spanwise separation of the high-speed regions does not appear to grow significantly with distance from the wall. At 1δ downstream, the signature of the structure is still quite strong, of similar strength as at $\Delta x = 0$.

The streamwise growth of the conditional structure is more clearly demonstrated in the two-dimensional plots of figure 8(b). Here, we show the x - z plane at $\Delta y = 0$ and five streamwise slices in the y - z plane, with both linear and logarithmic scalings of the z -axes. The linearly scaled y - z slices illustrate the approximately linear growth in height of the conditional contour levels with downstream location, with the location of the most strongly negative velocity moving further from the wall as we move downstream of the conditioning point. The development of the strong low-speed core of the superstructure is also clear, almost non-existent at $\Delta x = -\delta$, then rapidly gaining strength ($\Delta x = 0$ – 1δ) and again decaying to a weaker state at $\Delta x = 2\delta$. However, even at $\Delta x = 2\delta$ the general characteristics of the conditional average are still clearly evident and the overall structure remains very tall. This demonstrates the very large size and shallow inclination of the motions responsible for this conditional average, extending well over 2δ streamwise and above the mid-height of the boundary layer.

The logarithmic scaled slices reveal the consistency in structure width with wall-normal coordinate. The zero contour appears at a spanwise location of $\Delta y \approx \pm 0.25\delta$, suggesting that the width of the high-speed region located above a low skin-friction event is about 0.5δ . This width scale was also determined by examining a line plot along the spanwise direction (not shown for brevity). It could be argued that the width increases slightly upstream and downstream of the conditioning point, although the growth is marginal. One possible explanation for this widening could be the meandering of low-speed superstructures events as noted by Hutchins & Marusic (2007a), who showed (using synthetic structures) that such meandering could lead to widening of two-point correlations and also spectral widening in two-dimensional energy spectra (a redistribution of energy to larger λ_y as λ_x increases, as had been observed previously by del Álamo *et al.* 2004).

Although the spanwise and wall-normal components of the velocities are not measured in this study, results from DNS data (see del Álamo *et al.* 2006 and analysis in Hutchins & Marusic 2007b) suggest that the observed adjacent low- and high-speed regions are associated with a pair of counter-rotating roll modes. These roll modes sweep high-speed fluid to the wall and eject low-speed fluid away from the wall. The current results are entirely consistent with that study.

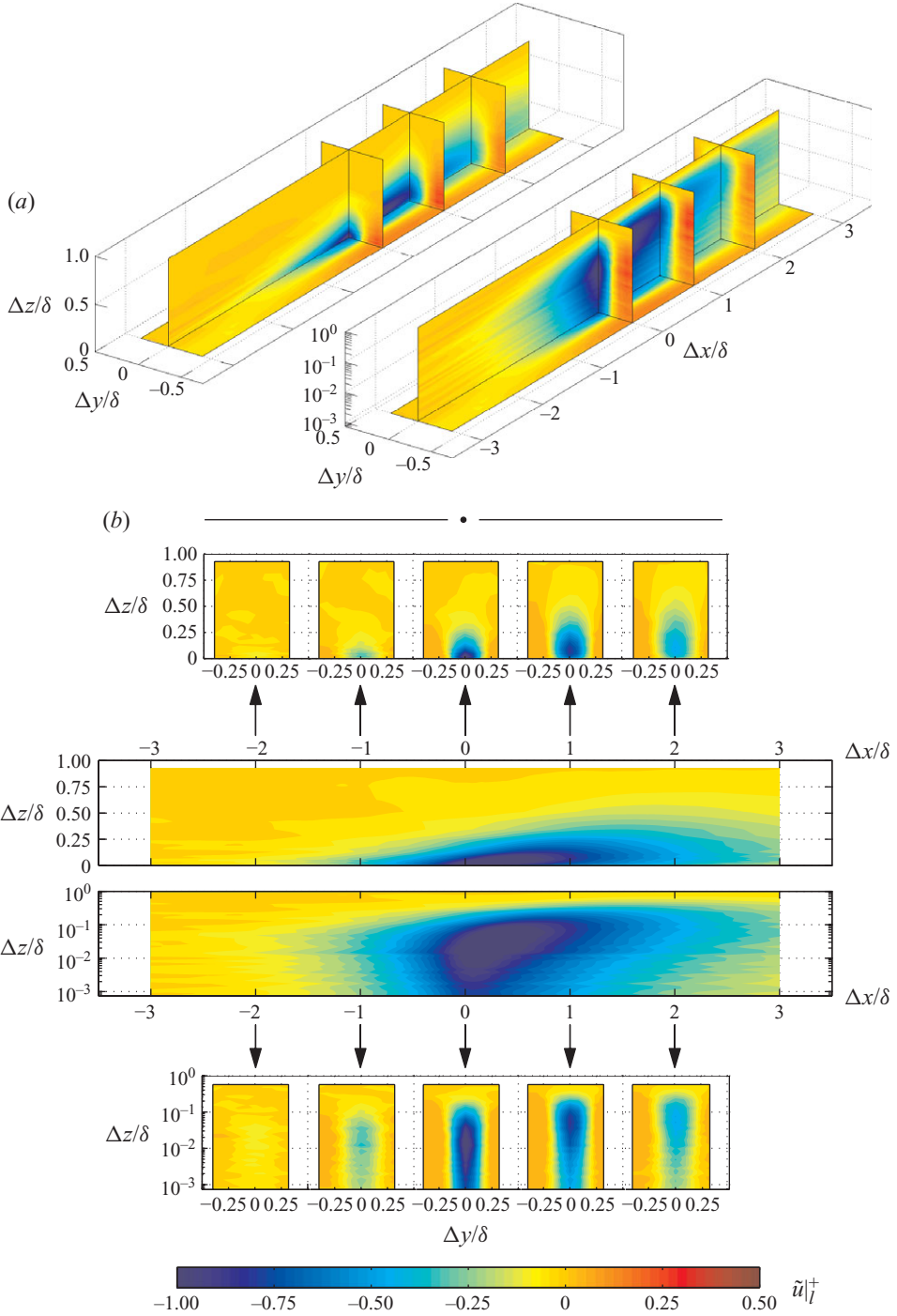


FIGURE 8. Iso-contours of the streamwise velocity conditionally averaged on a low shear-stress event. (a) Three-dimensional view of the x - y ($z/\delta = 7 \times 10^{-4} \approx 0$) plane, x - z plane and three y - z planes at locations of $x/\delta = 0, 1$ and 2 . (b) Two-dimensional views of x - z planes with y - z planes shown at five streamwise locations. In each figure, two sets of graphs are presented, one set with linear scaling and another with logarithmic scaling of the z -axis.

6.3. ‘Amplitude modulation’ of small-scale events

Bandyopadhyay & Hussain (1984), Hutchins & Marusic (2007b) and Mathis *et al.* (2009) have shown that large-scale structures in turbulent boundary layers can modulate the amplitude of the small-scale energy, and recently this has been the basis of a successful prediction model by Marusic, Mathis & Hutchins (2010). Here, we investigate this phenomenon by producing a conditional average of the small-scale component of the hot-wire signal, based upon the occurrence of a large-scale low skin-friction event at the wall. The first step in this analysis (as in Hutchins & Marusic 2007b; Mathis *et al.* 2009) is to decompose the hot-wire signal (hw2) into a small-scale component using a sharp spectral cutoff filter at $\lambda_x^+ \approx 7000$ (where λ_x is the streamwise wavelength). This filter size was shown by Hutchins & Marusic (2007b) to effectively separate the inner and outer peaks in the energy spectra of streamwise velocity fluctuations. The resulting filtered small-scale signal is called u_s . The conditional analysis is then completed in the same manner as in the previous section. The conditional event is the same (the occurrence of a large-scale negative skin-friction event), only in this case we ensemble average the change in small-scale variance:

$$\tilde{u}_s^2|_l(\Delta x, \Delta y, z) = \langle u_s^2(x, y, z) \mid u_\tau(x - \Delta x, y - \Delta y) < 0 \rangle - \overline{u_s^2}. \quad (6.5)$$

Note that in addition to the small-scale fluctuations having a zero mean ($\overline{u_s} = 0$), the mean of the small-scale fluctuations during a large-scale low or high skin-friction event is also zero ($\tilde{u}_s|_l = \tilde{u}_s|_h = 0$). Thus, the conditioned quantity $u_s^2|_l$, as defined in (6.5), is a true reflection of the conditional small-scale variance in the presence of a large-scale negative skin-friction fluctuation. Figure 9 presents three-dimensional views of the conditioned small-scale variance. The colour scale shows the change in conditioned small-scale variance as a percentage of the time-averaged unconditional small-scale variance, $(u_s^2|_l / \overline{u_s^2}) \times 100$. Red shading shows increased small-scale energy and blue shows reductions. The format of this figure is identical to figure 8 and a combination of plots with linear and logarithmic wall-normal axes is shown to display clearly the near-wall and outer region behaviour. With zero time-shift, Mathis *et al.* (2009) have shown that within a large-scale negative u fluctuation, the small-scale energy is attenuated close to the wall, but that this behaviour switches at $z^+ \approx \sqrt{15Re_\tau}$, above which point the small-scale energy is increased. Such behaviour is clearly evident in the conditional variance plots of figure 9. At $\Delta x = 0$, the reduced small-scale energy (blue contours) changes to increased small-scale energy (red contours) around $z^+ \approx 450$ (very close to $\sqrt{15Re_\tau}$ for the current Reynolds number). However, the wider three-dimensional view afforded by figure 9 shows that the crossover between reduced and increased small-scale energy is actually inclined in x . At $\Delta x \approx -\delta$, the crossover occurs very close to the wall, and at $\Delta x \approx \delta$ the crossover occurs at $z^+ \approx 1400$. A similar conditionally averaged contour plot of the small-scale variance associated with a large-scale negative u fluctuation is given by Bandyopadhyay & Hussain (1984) and more recently by Chung & Mckeon (2010). Note that the conditional analysis of figure 9 effectively shows the correlation between the amplitude of the local small-scale fluctuations at some given z -location and the large-scale skin-friction fluctuations at the surface. The analysis of Mathis *et al.* (2009) shows the correlation between the local small-scale amplitude at some given z -location and the large-scale velocity fluctuations at the *same* z -location. Thus, the measurements, whilst demonstrating a related phenomenon, are not directly equivalent or comparable.

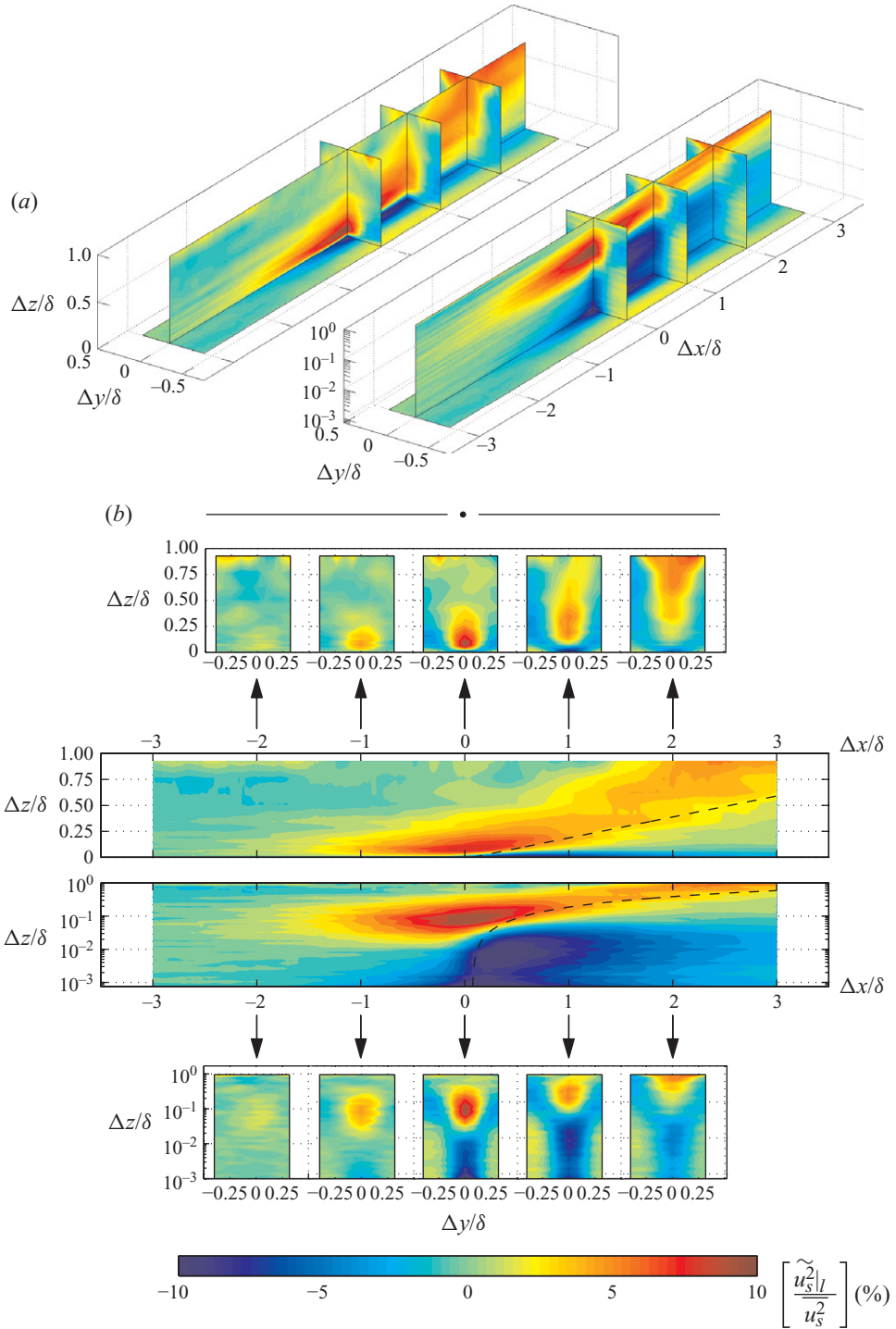


FIGURE 9. Iso-contours of percentage change in the streamwise small-scale velocity variance conditionally averaged on a low shear-stress event. (a) Three-dimensional view of the x - y ($z/\delta = 7 \times 10^{-4} \approx 0$) plane, x - z plane and three y - z planes at locations of $x/\delta = 0, 1$ and 2. (b) Two-dimensional views of x - z planes with y - z planes shown at five streamwise locations. In each figure, two sets of graphs are presented, one set with linear scaling and another set with logarithmic scaling of the z -axis. The dashed line on the x - z planes in (b) shows the streamwise minima of the conditioned velocity fluctuations from figure 8.

A careful comparison between figures 8 and 9 reveals that the separation between reduced and increased small-scale activity closely follows the local streamwise minima of the conditioned velocity fluctuations $\tilde{u}|_l$. The dashed line on the x - z planes of figure 9(b) shows the streamwise minima of the conditioned velocity fluctuations, which gives an almost linear trend inclined at approximately 11.5° (close to the large-scale inclination angles reported by Adrian, Meinhart & Tomkins 2000 and Marusic & Heuer 2007). This line is observed to very closely trace the separation between increased and reduced small-scale activity (the separation between red and blue contours). The streamwise minima of the conditioned velocity fluctuations are significant in that they demarcate a region of deceleration ($\partial_x u < 0$ upstream of the dashed line) from a region of acceleration ($\partial_x u > 0$ downstream of the dashed line). In short, figure 9 seems to indicate that increased small-scale activity might be associated with large-scale regions that exhibit streamwise decelerations, and conversely attenuated small-scale activity is associated with large-scale regions exhibiting local accelerations. It is worth mentioning at this point that although we here concentrate on the effect of streamwise velocity gradients, the inclined nature of the large-scale events enforces that a given streamwise gradient will be accompanied by anti-signed wall-normal gradients (i.e. $+\partial_x u$ will be accompanied by $-\partial_z u$ and vice versa). Thus, one could also attempt to explain modulation of small scales in terms of localised changes in the wall-normal velocity gradient.

6.4. Streamwise velocity gradient

On the basis of the above observations, we here examine the condition of a positive streamwise gradient in the filtered wall shear stress (i.e. the streamwise gradient of the footprint of a superstructure). The conditional average of velocity gradient at any point in the flow is therefore defined as

$$\widetilde{\partial_x u}|_{+ve}(\Delta x, \Delta y, z) = \langle \partial_x u | \partial_x u_\tau(x - \Delta x, \Delta y) > 0 \rangle \quad (6.6)$$

and the conditional average of variance as

$$\widetilde{u_s^2}|_{+ve}(\Delta x, \Delta y, z) = \langle u_s^2(x, y, z) | \partial_x u_\tau(x - \Delta x, \Delta y) > 0 \rangle - \overline{u_s^2}. \quad (6.7)$$

Observing figure 8, a positive $\partial_x u_\tau$ would be expected downstream of the condition point ($\Delta x > 0$), and a negative $\partial_x u_\tau$ would be expected for $\Delta x < 0$.

The conditional average of the velocity gradient based on positive $\partial_x u_\tau$ is shown for the streamwise-wall-normal plane at $\Delta y = 0$ in figure 10(a). The contours of the conditional velocity gradient are approximately linearly inclined at a similar angle as the conditional velocity contours shown previously in figure 8 (note the semi-logarithmic scaling of the figure). A relatively compact negative-positive-negative behaviour of the contours in the streamwise direction is exhibited. Two minima of $\partial_x u$ occur in the logarithmic region, separated by approximately 0.5 – 1.0δ in the streamwise direction. The peak positive gradient also occurs in the logarithmic region, at a location similar to the negative lobes (this is not visible in the figure due to the chosen contour levels). The upstream $\partial_x u^+$ minimum has a magnitude greater than 40% of the peak positive magnitude, making it a significant feature, while the downstream negative trough is somewhat weaker at 22%.

The importance of the region of strong positive streamwise velocity gradient is highlighted by its coincidence with the region of attenuation of the small-scale velocity fluctuations. This is illustrated in figure 10(b). The conditionally averaged small-scale variance is calculated on the occurrence of a positive skin-friction gradient (as given by (6.7)). This is plotted by solid line contours in figure 10(b), which show percentage

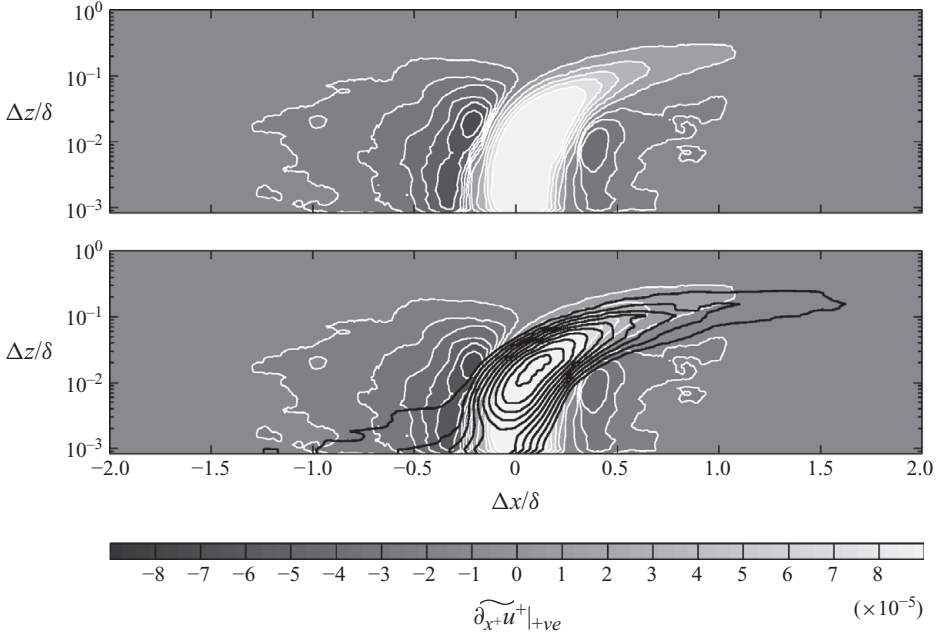


FIGURE 10. A large-scale event conditioned on the occurrence of positive $\partial_x u_\tau$ at the wall. Filled grey-shaded contours (with white outline) show $\partial_{x^+} u^+|_{+ve} > 0$ (white is positive $\partial_{x^+} u^+$ and darkest grey is negative $\partial_{x^+} u^+$, see grey scale below the figure). The solid black contours show regions in which the small-scale turbulence intensity is attenuated. Contours show $[\tilde{u}_s^2|_{+ve}/\overline{u_s^2}] \%$ from -10% to -1% in increments of 1% .

change in the small-scale variance $(\tilde{u}_s^2|_{+ve}/\overline{u_s^2}) \times 100$. The contours are plotted on top of shaded contours of the conditional velocity gradient event. The similarity between both sets of contours shown in figure 10(b) is striking. The streamwise gradient and small-scale variance conditional averages are both similarly inclined, albeit at slightly different angles. Although close to the wall, the coincidence of small-scale modulation with velocity gradient appears to degrade somewhat, they both in general occupy similar spatial regions. Most notably, the maximum velocity gradient occurs very close to the maximally attenuated small-scale variance. A similar relationship between the large-scale velocity gradient and the small-scale fluctuations has been observed in LES of turbulent channel flow (Chung & Mckeon 2010). In short, the modulation of small-scale energy within the turbulent boundary layer appears to be strongly associated with the large-scale streamwise velocity gradients brought about by the superstructure events. As highlighted in the previous section, the inclined nature of the large-scale events suggests that regions of streamwise velocity gradient are also accompanied by locally modified wall-normal velocity gradients.

Mathis *et al.* (2009) found that the correlation between the large scales and the envelope of the small-scale fluctuations switches sign close to the centre of the log region. A similar analysis (not shown here, but readily apparent from figure 10) reveals that in contrast the correlation between the gradient of the large-scale fluctuations $\partial u_L/\partial x$ and the envelope of the small-scale fluctuations will remain negative throughout the layer, which implies that the two remain in-phase (or similarly out of phase) throughout the layer.

The close spacing ($\lesssim 0.25\delta$) of the negative and positive velocity gradient peaks in figure 10(b) and general compactness of the contours is somewhat surprising. There appears no obvious reason from the conditional event $\tilde{u}|_l$ shown in figure 8 for such sharp transitions (spatially) from strong negative gradient to strong positive around the superstructure event. This transition certainly cannot be explained by evidence presented so far. However, in the following subsection, a further conditioning event is investigated, providing a possible interpretation of the gradient behaviour observed.

6.5. Meandering of the large-scale features

Although the conditional average of velocity fluctuation $\tilde{u}|_l$ shown in figure 8 implies the existence of streamwise velocity gradients, such gradients would neither be expected to be particularly strong nor compact. Recalling documented features of superstructures: the streamwise-aligned portion of superstructures consists of low-momentum regions flanked on either side by higher momentum regions. The magnitude of the difference between the high- and low-momentum regions is high (typically greater than $4U_\tau$) and occurs over distances of approximately 0.4δ in the spanwise direction (see, for example, figure 5). That is, the superstructures are characterised by strong *spanwise* gradients of streamwise velocity (strong $\partial_y u$). It was recognised by Hutchins & Marusic (2007a) that the superstructures of wall-turbulence meander in the spanwise direction as they travel downstream. Monty *et al.* (2007) also noted a strong meandering tendency in the very large scales of turbulent pipe and channel flows. It is plausible, therefore, that meandering of such superstructures could potentially lead to strong $\partial_x u$ as the strong *spanwise* gradients associated with the superstructure become partially realigned to the *streamwise* direction. Here, the meandering is investigated in greater detail using volumetric conditional averages. The purpose of this section is not necessarily to prove unequivocally that meandering of superstructure events occurs in turbulent boundary layers. Rather, what we seek to show, through a preliminary conditional averaging technique, is that meandering-type behaviour can lead to the strong large-scale streamwise gradients that appear to be closely correlated with the modulation of small-scale events.

Meandering is detected using the conditions illustrated in figure 11. Only meandering of large-scale *low* momentum regions is considered here for brevity. The condition events are essentially local regions of spanwise yawed, low skin-friction (the Gaussian-filtered skin-friction signals are used for these analyses). From the idealised example of a meandering streak shown in figure 11, it is clear that a condition criterion composed of low-speed events at the origin and opposing corners, flanked on either side by anti-signed streamwise velocity gradients, could potentially capture regions in the flow where meandering occurred. This detection scheme has been tested on filtered skin-friction data from the DNS data of del Álamo *et al.* (2004) and is proved to accurately detect low-friction events that are yawed in either the positive or negative y -direction. From these tests using DNS data, it is also clear that the streamwise separation over which the gradient is defined (0.4δ in figure 12) has very little effect on either the detected regions in the flow or the resulting conditional average. In addition, this detection scheme has been carefully tested on synthetic skin-friction fields. These synthetic fields were modelled as either meandering or straight idealised large-scale features (based on the synthetic structure suggested by Hutchins & Marusic 2007a) with superimposed smaller scale Gaussian noise. In these tests, the detection scheme has not only proved itself capable of extracting meandering features from the flow, but also demonstrated that the scheme does not give erroneous indications of meandering where none is present. The small-scale

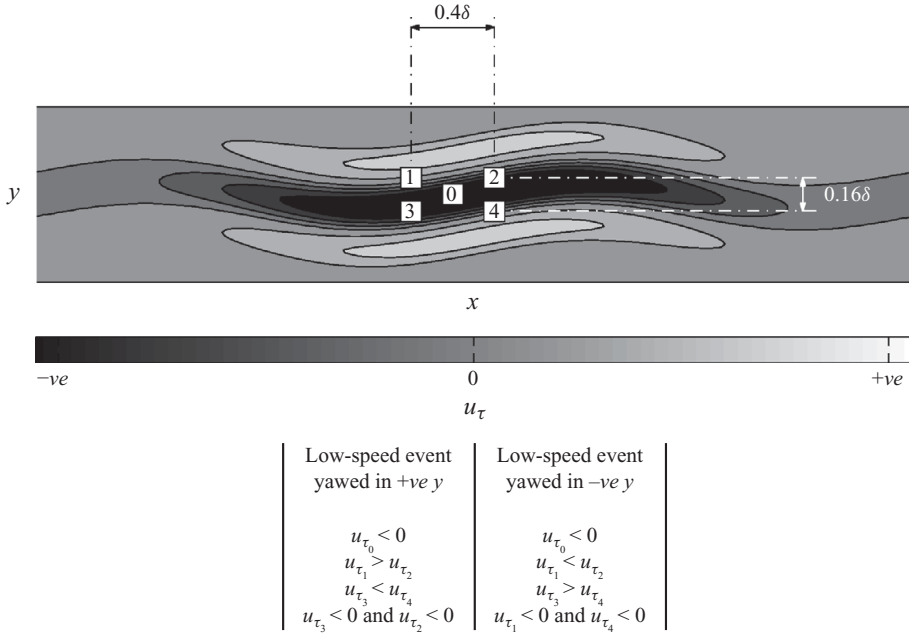


FIGURE 11. A new detection scheme for meandering streaks.

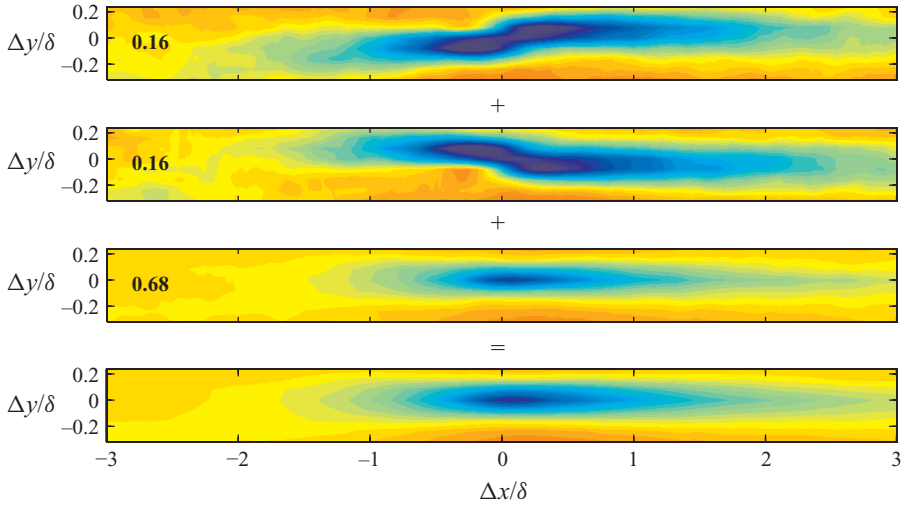


FIGURE 12. Conditional averages used to identify meandering behaviour. The figure illustrates the average nature of the meandering and how the overall low-momentum conditional average is made up of long meandering and straight features. Subfigures contain bold numbers indicating the average fraction of time that the various meandering behaviours are observed (given that a large-scale, low skin-friction event has occurred). Colour representation as in figure 8.

superimposed Gaussian noise only produces weak meandering features in the ensemble average which are spatially restricted to very compact and localised regions around the detection point. Where meandering large-scale structures are not present in the synthetic fields, there is no sign of large-scale meandering observed in the conditional averages produced from the detection scheme.

Figure 12 displays the streamwise–spanwise conditionally averaged velocity results for the lowest wall distance ($z^+ \approx 10$) given three conditions: (from top to bottom) meandering to the left, meandering to the right and no meandering (from the point of view of an observer facing downstream). The appropriately weighted meandering conditional averages in this figure must sum to the overall low-momentum conditional average (previously shown in figure 8 and shown as the lower plot of figure 12). The results confirm that meandering events are associated with long structures both upstream and downstream of the condition point. Moreover, the meandering large-scale structure is statistically stronger in magnitude (although less frequent) than the straighter structures. By the definition given in figure 11, the meandering events make up 32% of the total negative large-scale skin-friction events (of these 16% are inclined in the positive y -direction and 16% in the negative y -direction). The remaining 68% of the negative large-scale skin-friction events are comparatively straight. Thus, it is important to recognise that conditional averaging based solely on a negative skin-friction event at the origin (as shown in §6.2 and figure 8) will include a substantial portion of left- or right-leaning events (32% of the detection events would be classified as meandering). Such meandering, in addition to causing strong streamwise gradients (strong $\partial_y u$), will also lead to a shortening of streamwise wavelengths (λ_x) at which the spectral contribution of the largest scales appears. This has been demonstrated by Hutchins & Marusic (2007a), who compare one- and two-dimensional energy spectra for straight and meandering synthetic superstructure-type features, finding for the latter that the peak energy of streamwise fluctuations appears at substantially shorter λ_x .

To a certain extent, conditional averaging will always return a result that resembles the condition event (by definition, the detection criteria chosen must heavily influence the resulting conditional average). For example, in the current analysis, a negative fluctuation at the origin and opposing corners, coupled with anti-signed flanking gradients over $-0.2 < \Delta x/\delta < 0.2$, is enforced by the chosen conditioning scheme. However, if large-scale meandering structures were not statistically prevalent the conditional average would drop to zero rapidly beyond $|\Delta x| = 0.2$; this is not the case. Figure 12(a) also reveals strong gradients of streamwise velocity around the centre of meandering evidenced by sharp changes in colour from the darkest red to the deepest blue; compare conditional velocities $(\Delta x, \Delta y) = (-0.2\delta, 0.15\delta)$ to those at $(0.2\delta, 0.15\delta)$, for example. The chosen conditioning event has no thresholds imposed so that the observed strength of positive and negative velocities is also not enforced by the conditional-averaging scheme. These observations, together with the tests conducted on DNS data and synthetic fields, give confidence not only that the detection scheme is giving meaningful results but also that meandering superstructure-type events do seem to be statistically significant (particularly in terms of modulation of small-scale intensity).

6.6. Three-dimensional analysis of meandering events

As has been shown for the conditional mean velocity field in §6.2 and figure 8, it is possible to visualise the three-dimensional structure of velocity and variance in the vicinity of a conditional event, such as the meandering condition investigated here. In figure 13(a), the conditional average of mean velocity around a large-scale event meandering in the positive y -direction is displayed. In the central subfigure, an x – z plane at $\Delta y = 0.08\delta$ is shown to illustrate the behaviour of the flow in the streamwise direction in the region where the streamwise velocity gradient near the wall is strongest (i.e. where the large-scale structure meanders through the plane). It

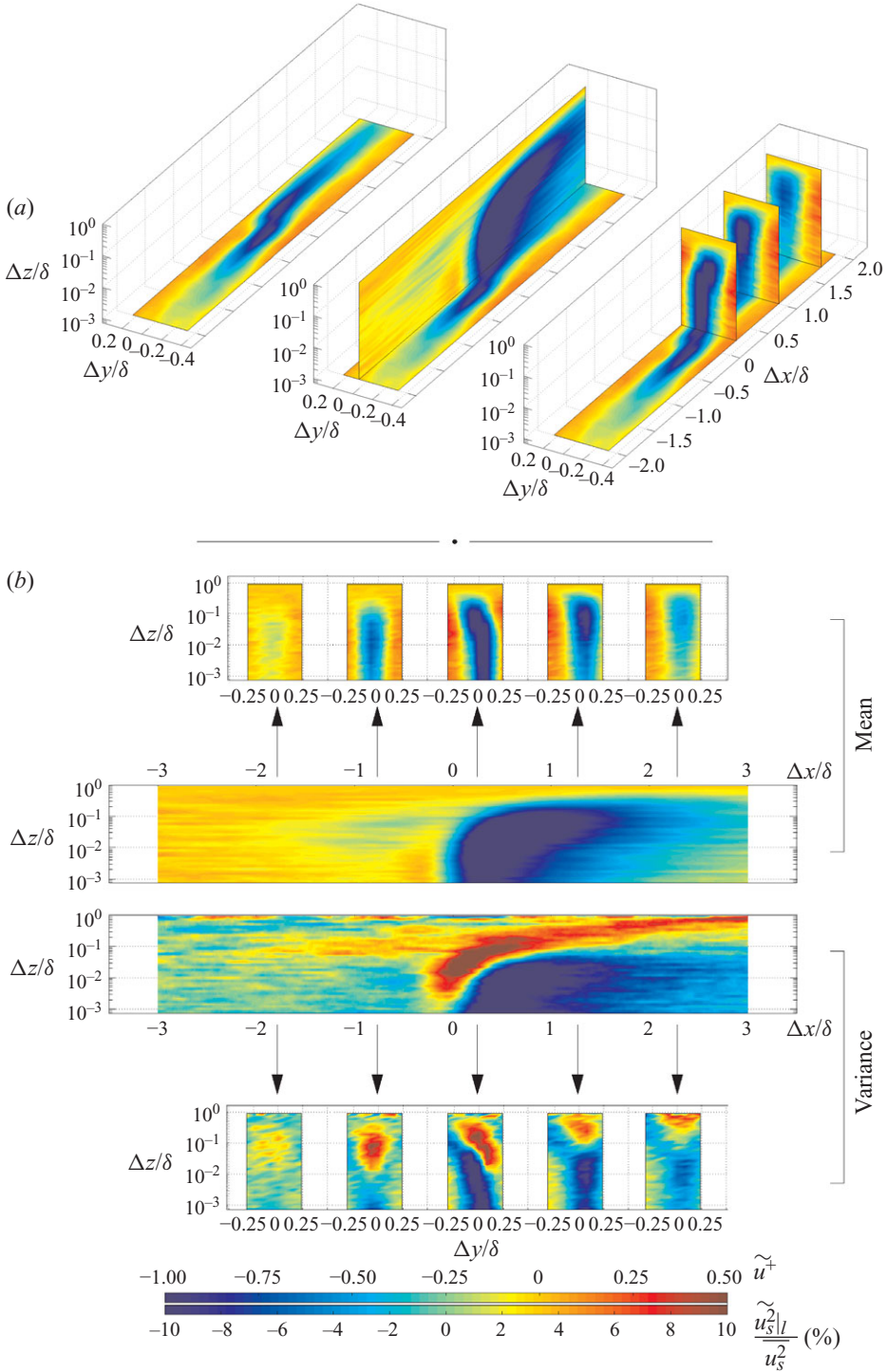


FIGURE 13. Iso-contours of the streamwise velocity and small-scale variance conditionally averaged on a meandering, low shear-stress event. (a) Three-dimensional view of the x - y ($z/\delta = 7 \times 10^{-4} \approx 0$) plane, x - z plane and three y - z planes at locations of $\Delta x = 0.25, 1.00$ and 1.75δ . (b) Two-dimensional views of x - z planes with y - z planes shown at five streamwise locations, $\Delta x = -1.75, -0.75, 0.25, 1.25, 2.25\delta$. Both conditional mean (as in a) and conditional small-scale variance are shown. Logarithmic scaling of the z -axis is employed throughout.

is clear that the meandering manoeuvre is associated with strong, relatively compact regions of streamwise velocity gradients $\partial_x u$ that extend from the wall to beyond the edge of the log region. Thus, we might reasonably conclude that meandering would strongly contribute to the conditional average based on skin-friction gradient as reported in §6.4 and figure 10.

In the rightmost subplot of figure 13(a), three y - z planes are shown at $\Delta x = 0.25, 1.0$ and 1.75δ to illustrate the development of the meandering large-scale structure away from the wall. It is interesting to note that the top of the structure appears to lag the lower portion as it meanders from right to left (i.e. particularly at $\Delta x = 0.25\delta$, where the low-speed region is noticeably inclined in the spanwise direction). To investigate this further, two-dimensional slices of the volumetric conditional average are shown in figure 13(b). From the streamwise-wall-normal planes, it is noted that the strong gradient associated with the meandering event is also inclined at the characteristic structure angle. This suggests that the entire meandering event is itself inclined, such that the most ‘kinked’ portion of the superstructure occurs downstream of the condition point for locations further from the wall. This gives rise to the spanwise leaning behaviour evident in the spanwise-wall-normal plots of figure 13(a). At this stage, the cause of the meandering is not clear, but figures 12 and 13 would seem to confirm that meandering is a statistically significant event and that perhaps the tendency to view large-scale events as purely streamwise aligned is somewhat misleading.

The lowermost plots of figure 13(b) present contours of the ensemble-averaged small-scale turbulent energy conditioned on the occurrence of a meandering large-scale skin-friction event (as a percentage change). A comparison between the upper and lower streamwise-wall-normal plots in figure 13(b) (a comparison between conditioned velocity fluctuation and small-scale activity) seems to reaffirm the previous observations from §6.4; namely that the magnitude of the small-scale fluctuations appears to be modulated by the presence of strong (and relatively compact) regions of streamwise velocity gradient. In this case, the meandering event has caused the superstructure to cross the streamwise-wall-normal plane, leading to a sharp inclined demarcation between positive and negative velocity fluctuation (strong streamwise velocity gradients). It is noted from the lower plot that the small-scale intensity is noticeably increased in the region of strong streamwise deceleration, and reduced in regions of streamwise acceleration.

In comparing conditional averages, such as those shown in figure 13, it should be emphasized that a constant convection velocity ($U_c^+ \approx 20$, as determined in §4) has been used to project the time-series data spatially. The precise length of the conditional events shown in figure 13 is a simple linear function of this convection velocity. Although the analysis of §4 gives confidence that the chosen value of U_c is an accurate reflection of the large-scale convection velocity, the choice of a constant U_c neglects the fact that convection velocity is to some degree expected to be scale-dependent (it is probable that the small scales convect at a rate different to the large-scale events, at least close to the wall). Though this is unlikely to substantially alter the principal results and conclusions, we remain open to the possibility that for plots such as figure 13, the convection velocity for the small-scale conditional average (lower plots of figure 13b) might be different from that of the large-scale conditional average (upper plots of figure 13b), and thus small errors may propagate through the x -axes of these figures.

7. Conclusions

A spanwise array of glue-on hot-film probes together with a traversing hot wire is used to identify the relationship between large-scale skin-friction fluctuations and

velocity fluctuations across the entire layer for a high-Reynolds-number turbulent boundary layer. Despite the well-known frequency response problems associated with glue-on thermal skin-friction sensors, careful initial validation experiments have proved the reliability of these sensors in adequately capturing the large-scale skin-friction fluctuations in the current facility. The ‘big and slow’ approach embodied by this facility (large boundary-layer thicknesses and relatively low free-stream velocities) ensures that the frequencies associated with the largest scales are relatively low (δ -scaled events are ~ 50 Hz and as such well within the usable frequency range of the sensors).

An initial experiment in which the array is streamwise aligned was conducted in order to compute the convection velocity of large-scale events. We find that the large-scale structures at the wall convect faster than the small scales. A scale-dependent convection velocity was recently reported by del Álamo & Jiménez (2009) and Monty & Chong (2009). It is also noted that at this particular Reynolds number, the convection velocity for the superstructure-type motions is closely matched to the mean velocity at $z^+ \approx \sqrt{15Re_\tau}$, which was previously suggested by Mathis *et al.* (2009) as the location of peak superstructure energy (equating to the geometric midpoint of the logarithmic region). In other words, the footprint of the superstructure convects at a velocity associated with the local mean at the midpoint of the logarithmic region.

The time-series fluctuating skin-friction data from the glue-on surface probes indicate the presence of structures that extend to large streamwise distances (over 6δ in length). Such skin-friction events appear to be the footprints of the large-scale superstructures that have previously been observed in the logarithmic region. A range of conditional mean and conditional variance analyses are performed to further understand the relationship between the large-scale skin-friction events and the velocity fluctuations in the boundary layer. The conditional mean results indicate the presence of a forward-leaning low-speed and high-speed structure above low and high skin-friction events, respectively (with flanking anti-signed behaviour).

The conditional values of small-scale turbulence intensity show that the low-speed structure associated with the low skin-friction event consists of weakened small-scale fluctuations near the wall switching to a regime of more intense small-scale fluctuations farther away from the wall. Conversely, the high-speed structure associated with high skin-friction events exhibit an opposite behaviour (intense small-scale activity near the wall, switching to weaker small-scale activity in the log region). It is observed that this behaviour is approximately aligned with changes in the streamwise velocity gradient of the conditional large-scale fluctuations. The crossover point in turbulence intensity coincides with the location where the streamwise gradient of the conditional large-scale fluctuations is zero (i.e. a local maximum/minimum in high/low skin-friction event). This observation is confirmed by producing a conditional average based on a gradient in the skin-friction fluctuations. Thus, it appears possible that increased small-scale activity is associated with large-scale features that produce local streamwise deceleration ($-\partial_x u$), and conversely attenuated small-scale activity is associated with regions where large-scale structures cause local accelerations or stretching ($\partial_x u$). It should also be noted that due to the inclined nature of the large-scale events, a positive streamwise gradient will also be accompanied by a reduced wall-normal velocity gradient (and vice versa). Hence, the modulation could also be explained, more generally, as occurring around the inclined shear layers associated with the large-scale structures. This notion is, in turn, consistent with the characteristic velocity deficit of the superstructures being wrapped by ‘shells’ of vorticity or vortical

structures, in a scenario similar to that reported by Adrian and coworkers (see for example Adrian *et al.* 2000) and more recently by del Álamo *et al.* (2006).

The conjecture is posed here that strong streamwise velocity gradients can arise when large-scale superstructure events meander in the spanwise direction. A conditioning scheme designed to detect meandering events is suggested and proved to be effective at capturing the velocity signature due to meandering events. Meandering is found to be a prevalent feature of superstructure events (according to our scheme, almost one-third of the detected superstructure events would be classified as meandering). It is confirmed that meandering of superstructure events can lead to very strong and compact regions of streamwise velocity gradient, and again it is noted that the modulation of small-scale intensity is closely aligned with such gradients.

As a more general concluding remark, these results confirm that small-scale structures, including near-wall streaks/vortices, are influenced by the passage of outer layer large-scale events (as previously observed by Bandyopadhyay & Hussain 1984; Hutchins & Marusic 2007*b*; Mathis *et al.* 2009). Therefore, any control strategy for high-Reynolds-number wall-bounded turbulence that aims to control the small-scale activity in the near-wall region (controlling the near-wall cycle of streamwise streaks/vortices) will probably need to account for the behaviour of the large-scale structures that are present in the outer layer. The results might also suggest the viability of specifically targeting the large-scale structure in order to control turbulence.

N.H., J.P.M. and I.M. acknowledge support from the Australian Research Council through grants DP0663499, FF0668703, DP0984577 and DP1093585. B.G. acknowledges the Royal Society for the travel grant that enabled his visit to the University of Melbourne. We also wish to thank the reviewers for their helpful comments.

REFERENCES

- ABE, H., KAWAMURA, H. & CHOI, H. 2004 Very large-scale structures and their effects on the wall shear-stress fluctuations in a turbulent channel flow up to $Re_\tau = 640$. *J. Fluids Engng* **126**, 835–843.
- ADRIAN, R. J., MEINHART, C. D. & TOMKINS, C. D. 2000 Vortex organization in the outer region of the turbulent boundary layer. *J. Fluid Mech.* **422**, 1–53.
- DEL ÁLAMO, J. C. & JIMÉNEZ, J. 2003 Spectra of the very large anisotropic scales in turbulent channels. *Phys. Fluids* **15** (6), L41–L44.
- DEL ÁLAMO, J. C. & JIMÉNEZ, J. 2009 Estimation of turbulent convection velocities and corrections to Taylor's approximation. *J. Fluid Mech.* **640**, 5–26.
- DEL ÁLAMO, J. C., JIMÉNEZ, J., ZANDONADE, P. & MOSER, R. 2004 Scaling of the energy spectra of turbulent channels. *J. Fluid Mech.* **500**, 135–144.
- DEL ÁLAMO, J. C., JIMÉNEZ, J., ZANDONADE, P. & MOSER, R. D. 2006 Self-similar vortex clusters in the turbulent logarithmic region. *J. Fluid Mech.* **561**, 329–358.
- ALFREDSSON, P. H., JOHANSSON, A. V., HARITONIDIS, J. H. & ECKELMANN, H. 1988 The fluctuating wall-shear stress and the velocity field in viscous sublayer. *Phys. Fluids* **31** (5), 1026–1033.
- BAILEY, S. C. C., HULTMARK, M., SMITS, A. & SCHULTZ, M. P. 2008 Azimuthal structure of turbulence in high-Reynolds-number pipe flow. *J. Fluid Mech.* **615**, 121–138.
- BALAKUMAR, B. J. & ADRIAN, R. J. 2007 Large- and very-large-scale motions in channel and boundary-layer flows. *Phil. Trans. R. Soc. Lond. A* **365**, 665–681.
- BANDYOPADHYAY, P. R. & HUSSAIN, A. K. M. F. 1984 The coupling between scales in shear flows. *Phys. Fluids* **27** (9), 2221–2228.
- BLACKWELDER, R. F. & KOVASZNY, L. S. G. 1972 Time scales and correlations in a turbulent boundary layer. *Phys. Fluids* **15**, 1545–1554.

- BROWN, G. R. & THOMAS, A. S. W. 1977 Large structure in a turbulent boundary layer. *Phys. Fluids* **20**, S243–S251.
- BRUUN, H. H. 1995 *Hot-Wire Anemometry*. Oxford University Press.
- CHUNG, D. & MCKEON, B. J. 2010 Large-eddy simulation of large-scale structures in long channel flow. *J. Fluid Mech.* **661**, 341–364.
- CLAUSER, F. H. 1956 The turbulent boundary layer. *Adv. Mech.* **4**, 1–51.
- DROBINSKI, P., CARLOTTI, P., NEWSOM, R. K., BANTA, R. M., FOSTER, R. C. & REDELSPERGER, J.-L. 2004 The structure of the near-neutral atmospheric surface layer. *J. Atmos. Sci.* **61**, 699–714.
- GANAPATHISUBRAMANI, B., CLEMENS, N. T. & DOLLING, D. S. 2006 Large scale motions in a supersonic turbulent boundary layer. *J. Fluid Mech.* **556**, 271–282.
- GANAPATHISUBRAMANI, B., CLEMENS, N. T. & DOLLING, D. S. 2007 Effects of upstream boundary layer on the unsteadiness of shock-induced separation. *J. Fluid Mech.* **585**, 369–394.
- GANAPATHISUBRAMANI, B., CLEMENS, N. T. & DOLLING, D. S. 2009 Low-frequency dynamics of shock-induced separation in a compression ramp interaction. *J. Fluid Mech.* **636**, 397–425.
- GANAPATHISUBRAMANI, B., LONGMIRE, E. K. & MARUSIC, I. 2003 Characteristics of vortex packets in turbulent boundary layers. *J. Fluid Mech.* **478**, 35–46.
- GUALA, M., HOMMEMA, S. E. & ADRIAN, R. J. 2006 Large-scale and very-large-scale motions in turbulent pipe flow. *J. Fluid Mech.* **554**, 521–542.
- HUNT, J. C. R. & MORRISON, J. F. 2000 Eddy structure in turbulent boundary layers. *Eur. J. Mech. B Fluids* **19**, 673–694.
- HUTCHINS, N. & MARUSIC, I. 2007a Evidence of very long meandering structures in the logarithmic region of turbulent boundary layers. *J. Fluid Mech.* **579**, 1–28.
- HUTCHINS, N. & MARUSIC, I. 2007b Large-scale influences in near-wall turbulence. *Phil. Trans. R. Soc. Lond.* **365**, 647–664.
- HUTCHINS, N., NICKELS, T. B., MARUSIC, I. & CHONG, M. S. 2009 Spatial resolution issues in hot-wire anemometry. *J. Fluid Mech.* **635**, 103–136.
- KIM, K. C. & ADRIAN, R. J. 1999 Very large-scale motion in the outer layer. *Phys. Fluids* **11** (2), 417–422.
- KOVASZNAVY, L. S. G., KIBENS, V. & BLACKWELDER, R. F. 1970 Large-scale motion in the intermittent region of a turbulent boundary layer. *J. Fluid Mech.* **41**, 283–326.
- KREPLIN, H. P. & ECKELMANN, H. 1988 Propagation of perturbations in the viscous sublayer and adjacent wall region. *J. Fluid Mech.* **95**, 305–322.
- KUNKEL, G. J. & MARUSIC, I. 2003 An approximate amplitude attenuation correction for hot-film shear stress sensors. *Exp. Fluids* **34** (2), 285–290.
- LIGRANI, P. M. & BRADSHAW, P. 1987 Spatial resolution and measurement of turbulence in the viscous sublayer using subminiature hot-wire probes. *Exp. Fluids* **5**, 407–417.
- MARUSIC, I. & HEUER, W. D. C. 2007 Reynolds number invariance of the structure inclination angle in wall turbulence. *Phys. Rev. Lett.* **99** (11), 114504.
- MARUSIC, I. & HUTCHINS, N. 2008 Study of the log-layer structure in wall turbulence over a very large range of Reynolds number. *Flow Turbul. Combust.* **81**, 115–130.
- MARUSIC, I., MATHIS, R. & HUTCHINS, N. 2010 Predictive model for wall-bounded turbulent flow. *Science* **329** (5988), 193–196.
- MATHIS, R., HUTCHINS, N. & MARUSIC, I. 2009 Large-scale amplitude modulation of the small-scale structures in turbulent boundary layers. *J. Fluid Mech.* **628**, 311–337.
- MONTY, J. P. & CHONG, M. S. 2009 Turbulent channel flow: comparison of streamwise velocity data from experiments and direct numerical simulation. *J. Fluid Mech.* **633**, 461–474.
- MONTY, J. P., STEWART, J. A., WILLIAMS, R. C. & CHONG, M. S. 2007 Large-scale features in turbulent pipe and channel flows. *J. Fluid Mech.* **589**, 147–156.
- NICKELS, T. B., MARUSIC, I., HAFEZ, S. & CHONG, M. S. 2005 Evidence of the k^{-1} law in high-Reynolds-number turbulent boundary layer. *Phys. Rev. Lett.* **95**, 074501.
- NICKELS, T. B., MARUSIC, I., HAFEZ, S., HUTCHINS, N. & CHONG, M. S. 2007 Some predictions of the attached eddy model for a high-Reynolds-number boundary layer. *Phil. Trans. R. Soc. Lond.* **265**, 807–822.
- PERRY, A. E., MARUSIC, I. & JONES, M. B. 2002 On the streamwise evolution of turbulent boundary layers in arbitrary pressure gradients. *J. Fluid Mech.* **461**, 61–91.

- RAO, K. N., NARASIMHA, R. & NARAYANAN, M. A. B. 1971 The phenomenon in a turbulent boundary layer. *J. Fluid Mech.* **48**, 339–352.
- RINGUETTE, M. J., WU, M. & MARTIN, M. P. 2008 Coherent structures in direct numerical simulation of turbulent boundary layers at Mach 3. *J. Fluid Mech.* **594**, 59–69.
- SCHLATTER, P., ORLU, R., LI, Q., BRETHOUWER, G., FRANSSON, J. H. M., JOHANSSON, A. V., ALFREDSSON, P. H. & HENNINGSON, D. S. 2009 Turbulent boundary layers up to $Re_\theta = 2500$ studied through simulation and experiment. *Phys. Fluids* **21** (5), 051702.
- SHOCKLING, M. A., ALLEN, J. J. & SMITS, A. J. 2006 Roughness effects in turbulent pipe flow. *J. Fluid Mech.* **564**, 267–285.
- TANAHASHI, M., KANG, S. J., MIYAMOTO, T., SHIOKAWA, S. & MIYAUCHI, T. 2004 Scaling law of fine scale eddies in turbulent channel flows up to $Re_\tau = 800$. *Intl J. Heat Fluid Flow* **25**, 331–340.
- TOMKINS, C. D. & ADRIAN, R. J. 2003 Spanwise structure and scale growth in turbulent boundary layers. *J. Fluid Mech.* **490**, 37–74.
- TSUBOKURA, M. 2005 LES study on the large-scale motions of wall turbulence and their structural difference between plane channel and pipe flows. In *Proc. of the Fourth Intl Symp. on Turbulence and Shear Flow Phenomena*. TSFP4, Williamsburg, Virginia.
- WARK, C. E. & NAGIB, H. M. 1991 Experimental investigation of coherent structures in turbulent boundary layers. *J. Fluid Mech.* **230**, 183–208.
- YOUNG, G. S., KRISTOVICH, D. A. R., HJELMFELT, M. R. & FOSTER, R. C. 2002 Rolls, streets, waves and more: a review of quasi-two-dimensional structures in the atmospheric boundary layer. *Bull. Am. Meteorol. Soc.* **83** (7), 997–1001.